TALLINN UNIVERSITY OF TECHNOLOGY
SCHOOL OF ENGINEERING
Department's title

CHARACTERIZATION OF Cu_2ZnSnS_4 MONOGRAIN POWDERS GROWN IN MOLTEN LiI, NaI, KI, RbI and CsI

Cu_2ZnSnS_4 MONOTERAPULBRITE SÜNTEESKASVATUS LiI, NaI, KI, RbI ja CsI SULADES SOOLADES

MASTER THESIS

Student name: Ali Fahad
Student code: 194307KAYM

Supervisor: Dr. Kristi Timmo
Senior Research Scientist

Co-supervisor Fairouz Ghisani
Early Stage Researcher

Tallinn 2021

(*On the reverse side of title page*)

AUTHOR'S DECLARATION

Hereby I declare, that I have written this thesis independently.
No academic degree has been applied for based on this material. All works, major viewpoints and data of the other authors used in this thesis have been referenced.

"....." 2021

Author: .....
/signature /

Thesis is in accordance with terms and requirements

"....." 2021

Supervisor: ….....
/signature/

Accepted for defence

"....."..... 2021 .

Chairman of theses defence commission: .....
/name and signature/

Non-exclusive licence for reproduction and publication of a graduation thesis[1]

I, Ali Fahad

1. grant Tallinn University of Technology free licence (non-exclusive licence) for my thesis "Characterization of Cu_2ZnSnS_4 monograin powders grown in molten LiI, NaI, KI, RbI and CsI"

supervised by senior research scientist Dr. Kristi Timmo

1.1 to be reproduced for the purposes of preservation and electronic publication of the graduation thesis, incl. to be entered in the digital collection of the library of Tallinn University of Technology until expiry of the term of copyright;

1.2 to be published via the web of Tallinn University of Technology, incl. to be entered in the digital collection of the library of Tallinn University of Technology until expiry of the term of copyright.

2. I am aware that the author also retains the rights specified in clause 1 of the non-exclusive licence.

3. I confirm that granting the non-exclusive licence does not infringe other persons' intellectual property rights, the rights arising from the Personal Data Protection Act or rights arising from other legislation.

21.05.2021 (date)

[1] *The non-exclusive licence is not valid during the validity of access restriction indicated in the student's application for restriction on access to the graduation thesis that has been signed by the school's dean, except in case of the university's right to reproduce the thesis for preservation purposes only. If a graduation thesis is based on the joint creative activity of two or more persons and the co-author(s) has/have not granted, by the set deadline, the student defending his/her graduation thesis consent to reproduce and publish the graduation thesis in compliance with clauses 1.1 and 1.2 of the non-exclusive licence, the non-exclusive license shall not be valid for the period.*

Department of Materials and Environmental Technology

THESIS TASK

Student: Ali Fahad, 194307KAYM

Study programme, KAYM09, Materials and Processes for Sustainable Energetics

main speciality: Materials for Sustainable Energetics

Supervisor(s): Senior Researcher, Dr. Kristi Timmo, +372 6203362

Consultants: ……..(name, position)

…… (company, phone, e-mail)

Thesis topic:

(in English) Characterization of Cu_2ZnSnS_4 monograin powders grown in molten LiI, NaI, KI, RbI and CsI

(in Estonian) Cu_2ZnSnS_4 monoterapulbrite sünteeskasvatus LiI, NaI, KI, RbI ja CsI sulades soolades.

Thesis main objectives:

1. Synthesis-growth of Cu_2ZnSnS_4 monograin powders in five different flux materials such as CsI, RbI, LiI, NaI and KI.

2. Characterization of synthesized materials by analysing phase composition (X-ray diffraction and Raman analysis), morphology (by scanning electron microscope), elemental composition (by energy dispersive X-ray spectroscopy) and device characterization (by I-V curve and quantum efficiency measurements).

Thesis tasks and time schedule:

No	Task description	Deadline
1.	Synthesis-growth of Cu_2ZnSnS_4 monograin powders in five different flux materials such as CsI, RbI, LiI, NaI and KI	01.10.2020
2.	Characterization of synthesized materials by analysing phase composition (X-ray diffraction and Raman analysis), morphology (by scanning electron microscope), elemental composition (by energy dispersive X-ray spectroscopy) and device characterization (by *I-V* curve and quantum efficiency measurements).	01.04.2021
3.	Writing Thesis	20.05.2021

Language: …… **Deadline for submission of thesis:** "....."..... 201….a

Student: …….. ..... "....."…….....2021-a

/signature/

Supervisor: …… …….. "....."…….....2021-a

/signature/

Consultant: …… …..... "....."…….....2021-a

/signature/

Head of study programme: …… ..... "....."…….....2021-a

/signature/

Terms of thesis closed defence and/or restricted access conditions to be formulated on the reverse side

TABLE OF CONTENTS

PREFACE

The thesis topic "Characterization of Cu_2ZnSnS_4 monograin powders grown in molten LiI, NaI, KI, RbI and CsI" was proposed by my supervisor, senior researcher Dr. Kristi Timmo. All the experimental work done with respect to this thesis was carried out in the Laboratory of Photovoltaic Materials at the Department of Materials and Environmental Technology, Tallinn University of Technology. This work was supported by the Estonian Research Council project PRG1023, by ERDF project „Center of nanomaterials technologies and research (NAMUR+)" (2014-2020.4.01.16-0123), by the European Union through the European Regional Development Fund, Project TK141 and by European Union's H2020 research and innovation programme under Grant Agreement nº 952982.

I would like to thank my supervisor, Dr. Kristi Timmo, for the patient guidance, encouragement and advice she has provided throughout my time as her student. I have been extremely lucky to have a supervisor who cared so much about my work, and who responded to my questions and queries so promptly. I thank my co-supervisor Fairouz Ghisani (PhD Student) for her assistance from the very day one of this thesis to the final day. In addition, I would also like to thank other research group members – Dr. Marit Kauk-Kuusik, Dr. Maris Pilvet and Dr. Mare Altosaar. Furthermore, I am grateful for the team that assisted me in the characterization measurements namely – Dr. Valdek Mikli, Dr. Maarja Grossberg and Dr. Mati Danilson, whose support were necessary to compute the results. Finally, I want to thank my family for their support, goodwill and prayers that kept me afloat.

In this study, Cu_2ZnSnS_4 (CZTS) monograin powder materials were synthesized from binary chalcogenides and elemental sulfur in the liquid phase of different flux materials such as cesium iodide (CsI), rubidium iodide (RbI), lithium iodide (LiI), sodium iodide (NaI) and potassium iodide (KI). The main objective of this study was to investigate and compare the effect of different flux materials on pure Cu_2ZnSnS_4 monograin powder properties with the aim to increase the performance of monograin layer solar cells. Based on the results of this study, it was concluded that Li^+ from the molten flux (LiI) incorporated into the Cu_2ZnSnS_4 crystals structure and most probably, by replacing part of Cu^+ sites in the lattice formed new $(Cu_{1-x}Li_x)_2ZnSnS_4$ solid solution. The monograin layer solar cells prepared from Cu_2ZnSnS_4 powders grown in potassium iodide (KI) flux presented the best solar cell efficiency of 6.12%.

Keywords: kesterite, Cu_2ZnSnS_4, molten salt synthesis-growth, monograin powder technology, solar cell

List of abbreviations and symbols

CTZS	Copper Zinc Tin Sulfide
CsI	Cesium Iodide
RbI	Rubidium Iodide
LiI	Lithium Iodide
NaI	Sodium Iodide
*Eg**	Effective band gap energy
EDX	Energy-dispersive X-ray spectroscopy
EQE	External Quantum Efficiency
FF	Fill Factor
Hwhm	half width at half maximum
J_{sc}	Short circuit current density
KI	Potassium Iodide
MGL	Monograin layer solar cell
MGP	Monograin Powder
PV	Photovoltaics
PCE	Power conversion efficiency
QE	Quantum Efficiency
SEM	Scanning electron microscopy
V_{oc}	Open-circuit voltage
XRD	X-ray diffraction

INTRODUCTION

The world's key energy supplies are non-renewable and face increasing demand, so they are not likely to last for too long. These outlets, in addition to being non-renewable, largely consist of fossil fuels, which contribute greatly to the current global warming crisis. Due to the significant scarcity and pollution problems of the above energy sources, the international community's focus on alternative energy sources, especially solar energy, appears to be highly promising [1].

The word "renewable energy" is energy extracted from a wide range of materials, all of which are dependent on self-renewing energy sources such as sunshine, wind, moving water, the earth's internal heat, and biomass such as energy crops, agricultural and industrial waste, and urban waste. These sources can be used to generate electricity for all economic industries, fuels for transportation, and heat for buildings and manufacturing processes [2].

Solar energy, among other renewable energy sources, is a promising and readily available source of energy. Solar cells are renewable energy sources free of emissions that can easily replace conventional fossil fuels. A technique for converting sunlight directly into energy using solar cells is called Photovoltaic. In the last few years, the photovoltaic market has grown by 40 percent annually [3][4]. Currently, mc-Si and pc-Si technologies account for more than 80% of the solar cell industry. However, the production of silicon-based solar cells requires a significant amount of energy and materials. Thin film solar cells are a type of solar energy harvesting technology that offers a cost-effective and scalable method of harnessing solar energy. Cu(In,Ga)Se2 (CIGS) and CdTe solar cells have attained conversion efficiencies of over 21% and have been successfully industrialized among thin film solar cells [5]. However, there is considerable concern about the global supply of indium (In) and tellurium (Te), both of which are needed for CIGS and CdTe solar cells. Furthermore, cadmium (Cd) is toxic, prompting questions about the environmental effects of its treatment after use [5].

Cu_2ZnSnS_4 (CZTS), $Cu_2ZnSnSe_4$ (CZTSe), and their solid solutions $Cu_2ZnSn(S,Se)_4$ (CZTSSe) are made up of non-toxic and earth abundant elements, making them a low-cost and environmentally friendly absorber materials for thin film solar cells. The growth mechanism and properties of CZTSSe materials have been investigated in great detail, however recorded maximum efficiency value 12.6 % is quite low compared with CIGSe or CdTe thin film soral cells. The phase purity, electronic and optical properties of the absorber layer are critical and in dependence of the preparation technology as they directly affect the efficiency of CZTSSe solar cells [5].

Molten salt synthesis-growth method is one possibility for producing very high-quality absorber materials for solar cells. Molten salt medium (liquid phase of flux material) increases content diffusion, and as a result, the creation of a more homogeneous substance material is expected in comparision with solid state reaction method. On the ohter hand, doping impurities can be found in the liquid form of flux which are easily incorporated in the crystal during growth process.

The objective of this study is to investigate and compare the effect of different flux materials such as lithium iodide (LiI), sodium iodide (NaI), rubidium iodide (RbI), cesium iodide (CsI) and potassium iodide (KI) on pure sulfide (CZTS) monograin powder properties with the aim to increase the performance of monograin layer solar cells. The thesis is based on the experimental work carried out in the Laboratory of Photovoltaic Materials, at the Department of Materials and Environmental Technology, in Tallinn University of Technology.

1 LITERATURE REVIEW

1.1 Photovoltaic technology

Photovoltaic is a technology that generates electrical energy measured in watts (W) or kilowatts (kW) of the semiconductor when illuminated by photons. Electric power is produced continuously if the sun shines on a solar panel; it provides electrical power. The energy will be produced before the light ceases. The solar cell is very different from the battery, it does not need to be recharged.

It consists of semiconductors with weakly bonded electrons bearing a band of energy called the valence band. Bonds are dissolved until a threshold is exceeded. The energy difference of the band is associated with the valence electron. It has a degree of freedom of movement across a new energy band called the conduction band, where it can "beam" power through the material. Thus, the free electron in the conduction band may be separated by a bandage from the valence band; (measured in units of electron volts or eV). Photons that are light particles will provide this energy, which is necessary for the release of an electron [6].

1.2 Principal of solar cells

Solar cells are composed of semiconductors., which are materials with electrons with weak bonds that exist in an energy band known as the valence band. When energy is added to a valence electron that exceeds a certain threshold, called the band gap energy, the electron is "free" when the bonds have been broken and pass in a different energy band called the conduction band, where it is possible for electricity to pass through the substance. The band difference separates the free electrons in the conduction band from those in the valence band ((unit measurement is electron volts (eV)) [6].

A solar cell has a PN junction with a wide surface region. (Figure 1.1). The N-type material is kept thin to allow light to move through to the PN junction. Light travels in the form of photons, which are energy bags. The depletion field of the PN junction is where electric current is generated. The depletion zone is the region around the PN junction where electrons from the N-type material have diffused through the P-type material's holes. As a photon of light is absorbed by one of these N-type substance atoms, it displaces an electron, leaving a free electron and a vacuum in the process. The energy of the free electron and hole is sufficient to enable them to escape the

depletion field. Electrons can travel through a wire that connects the cathode (N-type material) to the anode (P-type material). The electron is drawn to the P-type material's positive charge and passes through the external load (meter), producing an electric current. The hole created by the ejected electron is attracted to the N-type material's negative charge and migrates to the back electrical contact. As the electron enters the P-type substance from the back electrical contact, it combines with the hole, preserving electrical neutrality. [7].

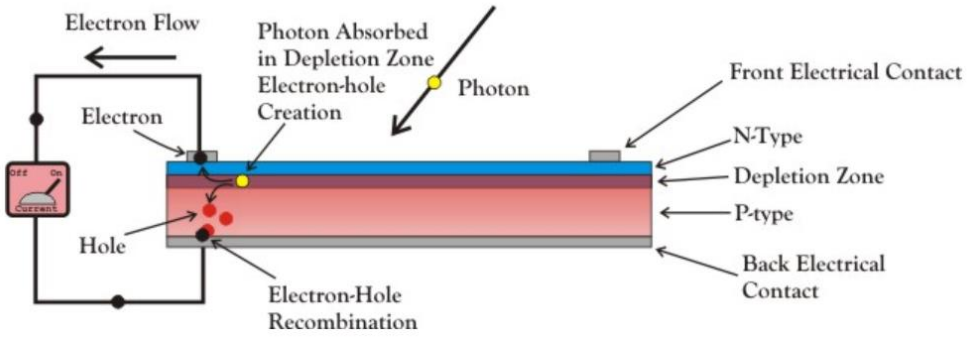

Figure 1.1 A simple structure of a photovoltaic cell [7].

Photons, which are light rays, can provide the energy required to release the electron. Figure 1.2 illustrates the schematic of a solar cell. As photons collide with valence electrons in a solar cell, the bonds between them are dissolved, and the electrons are pumped to the conduction band. A specially engineered selective contact collects conduction-band electrons and transports them to an external circuit. The electrons lose energy as the current is released, but they are returned to the solar cell by the circuit's return loop, which uses a second selective touch to return them to the valence band with the same energy they had before.

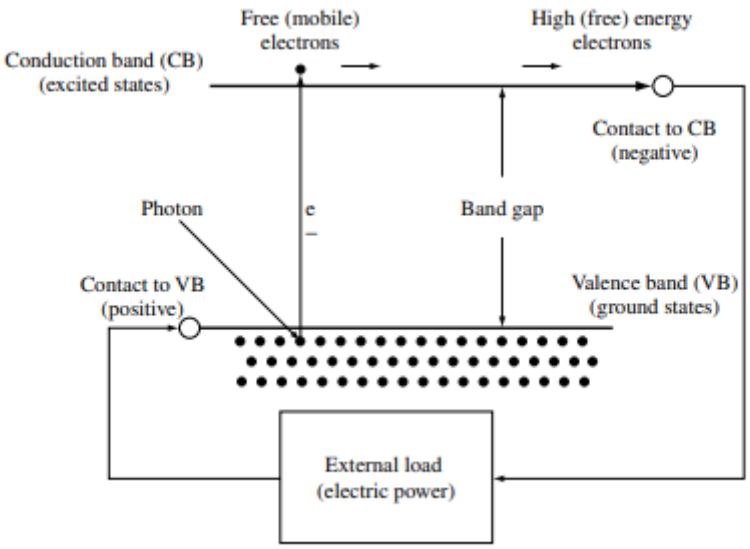

Figure 1.2 Schematic of a solar cell [6].

The electric current is the passage of these electrons in the external circuit and interactions. The band gap is the difference in potential between the potential at which electrons are released into the outer universe and the potential at which they are trapped, as well as the threshold frequency at which they were excited. Thus, electrons excited by a 2 eV photon or a 3 eV photon will each have a potential of somewhat less than 1 V in a medium with a 1 eV band difference (i.e. the electrons are delivered with an energy of 1 eV). The product of current and voltage is the electric power generated; that is, power is the number of free electrons multiplied by their potential [6].

1.3 Overview of absorber materials

The assessment of the solar cell generally must satisfy three essential requirements i.e. absorption coefficient (to capture photons efficiently and generate pairs of electron-hole), strong charge carrier transport properties (to harvest before recombination photo generated carriers) and a high and unifrom internal electric field (to maintain pair isolation of electron-hole at the PN junction) [8]. The band gap energy value of ssemiconductor materials has also a big impact on the solar cell's performance. In order to produce effective, robust, low-cost and heterojunction solar cells with a broad band gap window layer and a narrow band gap absorber layer are currently the subject of intense study [9]. The selection of ideal photovoltaic absorber materials is constrained by the photovoltaic material's bandgap matching the solar spectrum, which ranges between 1.1 and 1.5 eV. This range includes silicon (Si, 1.12 eV), gallium arsenide

(GaAs, 1.42 eV), cadmium telluride (CdTe, 1.49 eV), and copper indium gallium selenide (CIGS, 1-1.7 eV), which are the main materials for solar cells at the moment [10].

1.4 Kesterite type materials

$Cu_2ZnSn(S,Se)_4$ semiconductor materials with kesterite structure are among the potential absorber layer candidates for solar cells, also they have a variable direct band gap between 1.0 to 1.5 eV and high absorption coefficient, ($\alpha > 10^4$ cm^{-1}) [11].

1.4.1 Kesterite based solar cells

CZTS was first studied as a solar cell substance at Shinshu University in Japan in 1988. The first CZTS thin films were deposited by researchers using sputtering technology and *p*-type conductivity, a direct band gap of 1.45 eV, and absorption coefficients above 10^4 cm^{-1} in the visible range were detected [11]. The first solar cells with efficiencies greater than 0.6 % based on CZTS and CZTSe absorbers and cadmium sulfide/zinc oxide window layers were published in 1996 [12]. Further studies continued over the next decade, enhancing processing conditions and window layers, resulting in efficiencies up to 7%. [13]. In 2013, the Watson Research Center of IBM was able to push the performance of a lab-scale solar cell to 12.6% using a hydrazine-based solution technique, which is still the world record for a CZTSSe-based solar cell [14]. The conversion efficiency depends on different parameters such as growth condition, crystalline quality, *p-n* junction nature, carrier concentration, etc. Furthermore, the formation of secondary phases in the absorber layer limits the device performance. However, it was discovered that a slightly Zn-rich absorber layer produces higher efficiencies. The buffer layer is another significant constraint that will influence performance. Until now, high-efficiency solar cells have been made using a CdS buffer layer. The ZnS buffer layer has a large band offset, while Zn(O,S) has good performance [15] [16].

CZTSSe thin film solar cells have a structure that is identical to that of CIGS thin film solar cells. The structure as shown in Figure 1.3 is made up from bottom to top, with Mo deposited on SLG as the back contact electrode, CZTSSe absorber layer, CdS buffer layer, i-ZnO window layer, ZnO:Al clear conductive layer, and Ni/Al grid lines. Via a buffer layer and a translucent conductive layer, holes are transferred from the CZTSSe valence band maximum (VBM) to the back contact, and electrons are transferred from the conduction band minimum (CBM) to the Ni/Al grid lines via buffer layer and transparent conductive layer [17].

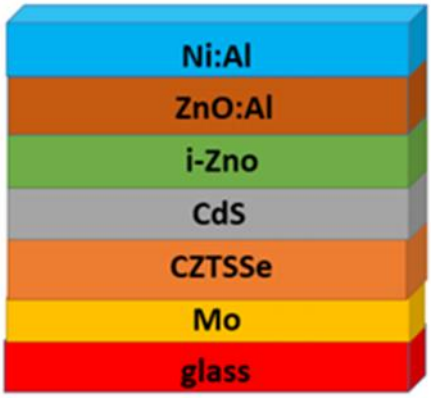

Figure 1.3 Basic structure of CZTSSe thin film solar cell [17].

1.4.2 Crystal structure of kesterite

Kesterite structure of CZTSSe is derived from the chalcopyrite-type structure of $Cu(In,Ga)Se_2$ (see Figure 4). As Zn and Sn elements in group II and IV replace In and Ga elements in group III in CIGS, the quaternary semiconductor compound I_2-II-IV-VI_4 (CZTSSe) is formed. Thus, CZTSSe and CIGS should show quite similar structural and material properties. However, compared with the binary and ternary semiconductors, the properties of CZTSSe are more complicated [9].

CZTS can take several type of crystal structures. The CZTS shows two structures fundamentally kesterite (space group $I\bar{4}$) and stannite (space group $I\bar{4}2m$). Due to alternating positioning of cations in the crystal lattice, the stannite structure has the same tetragonal coordination but a different symmetry. These two structures having different arrangements of Cu and Zn atoms in the crystal structure, see Figure 1.4 [20]. Furthermore, there is a disordered kesterite phase, in which the copper and zinc atoms in the kesterite structure are ununiformly distributed [18].

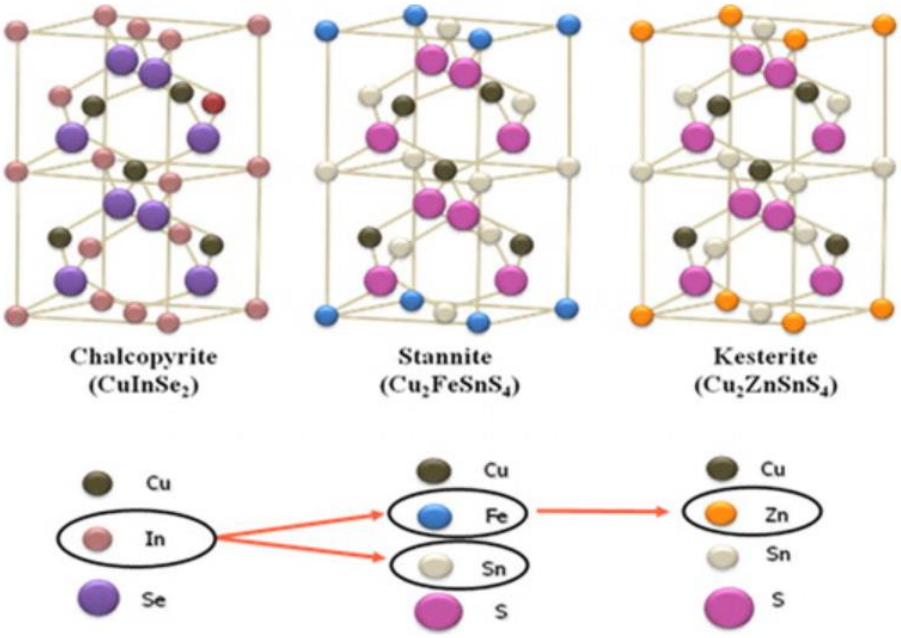

Figure 1.4 Schematic representation of chalcopyrite, stannite and kesterite structure [18].

1.4.3 Defect studies in kesterites

In experimental and theoretical studies of kesterites, intrinsic point defects and related band tailing have been established as the primary limiting factors causing the significant V_{oc} deficit. According to photoluminescence (PL) measurement reports, the majority of kesterite materials exhibit behaviours that are characteristic of heavily doped and compensated semiconductors [19].

The high doping in kesterites is caused by a very high concentration of charged intrinsic defects ($>10^{20}$ cm^{-1}), which extending the defect levels outside the forbidden gap causes spatial potential fluctuations and the forming of band tails. In a *p*-type material with a low effective mass for electrons, such as kesterites, radiative recombination can occur primarily across four channels: band-to-tail recombination (BT), which involves a free electron and a hole localized in the valence band tail; band-to-band recombination (BB), which involves a free electron and a free hole; band-to-impurity (BI) recombination that involves an acceptor state that is deep enough not to overlap with the valence band tail, and donor–acceptor pair (DAP) recombination that involves an acceptor and a donor state that are deep enough not to overlap with the corresponding band tails. All of these recombination mechanisms have been identified in kesterite PL tests. In addition to the spatial electrostatic potential fluctuations, kesterites have negative band gap fluctuations caused by the systemic Cu-Zn disorder and compositional inhomogeneities, lowering the V_{oc} of the corresponding solar cell units [20]. Cu_{Zn} is the dominant *p*-type defect in the stable chemical potential spectrum, with lower energy than Cu vacancy.

There are several potential defect complexes in the quaternary structure due to the presence of three cations. The bound anti-site pair of Cu and Zn has a particularly low energy, which can result in the formation of CZTS polytype structures. Under Zn-rich and Cu-poor conditions, the formation of the $[V_{Cu}^{-}+Zn_{Cu}^{+}]^{0}$ pair should be advantageous for optimizing solar cell performance; however, ZnS precipitation must be avoided [21]. Figure 1.5 summarizes the measured intrinsic defect ionization levels within the band gap of Cu_2ZnSnS_4.

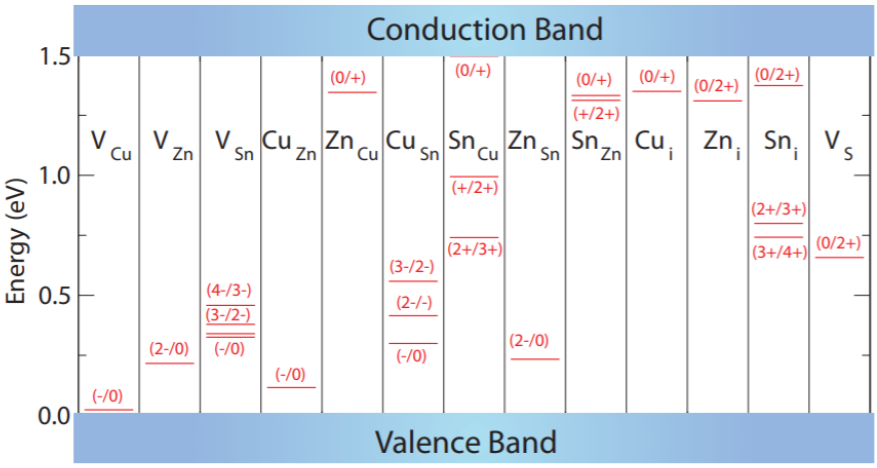

Figure 1.5 Calculated transition energy levels of intrinsic defects in the band gap of Cu_2ZnSnS_4 [22].

Biswas *et al.* [23], based on higher energy (less abundant) Sn defects, emphasizing that the corresponding donor states are deep, owing to the accessibility of both Sn(II) and Sn(IV) oxidation states. The presence of both oxidation states is well known, and it is linked to the fact that Sn has two valence states, one with a low energy 5s and the other with a higher energy 5p. When the Sn 5p state is filled, the energy level rises. This explains why Sn_{Cu} (0/+) is a shallow donor standard and why it is higher than Sn_{Zn} (0/+), despite the fact that the valence gap, and thus the electronegativity differential, between Sn and Cu is greater [22].

1.4.4 Effect of alkali metals (Li, Na, K, Rb, Cs) doping on kesterite solar cells.

Alkali treatment of kesterite solar cells is one of the steps used to minimize the high *Voc*-deficit, and the majority of today's >10% quality kesterite systems take advantage of the beneficial effects of alkali elements on absorber layer morphology and optoelectronic properties [24].

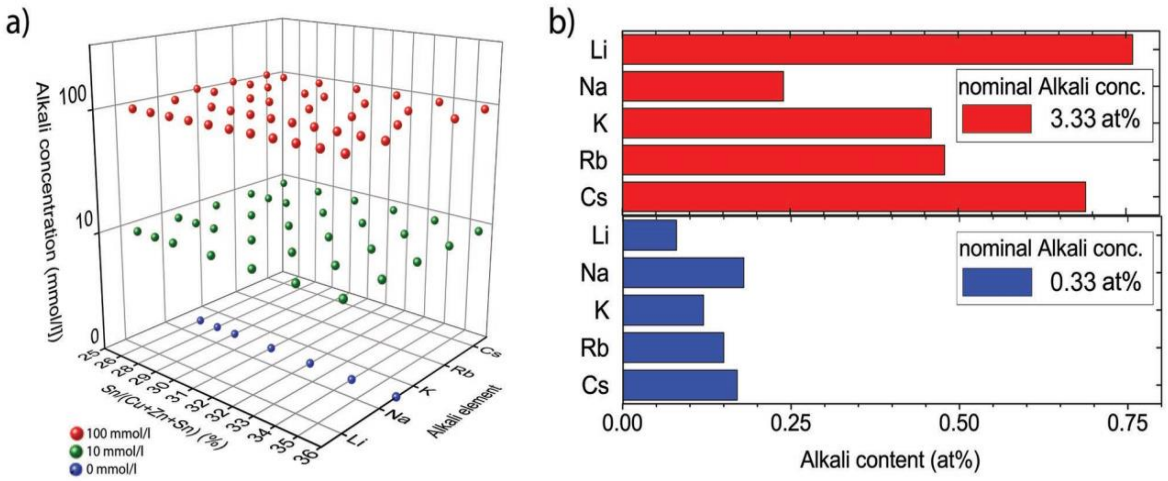

Figure 1.6 a) All samples fabricated for this study are depicted in dependence of the alkali element, alkali concentration, and Sn content. b) Comparison of the nominal alkali concentration with the alkali content determined by ICP-MS measurements [24].

The five separate alkali elements were used to build a matrix of sample compositions.: lithium (Li), sodium (Na), potassium (K), rubidium (Rb), and cesium (Cs) is shown in Figure 1.6 a. The nominal alkali concentration in the precursor solution was varied in three phases of 0, 10, and 100 pH. Changing the Sn concentration in the precursor Solution in up to 12 steps resulted in changes in metal ratios [24]. Figure 1.6 b indicates the calculated concentrations of all five alkali elements. Intentionally inserted alkali elements are effectively integrated into the absorber layer. The majority of the alkali quantity escapes during processing. ICP-MS measurements show that, with the exception of Li, heavier alkali. elements remain at higher concentrations within the absorbber layer than lighter elements. The total amount is expected to be higher for samples with a higher density of grain boundaries. The alkali-containing samples of 10 pH (0.33 percent) and 100 pH (3.33%) would be referred to as "low" and "high" alkali content, respectively, in the following examples [24].

Doping is commonly used to describe a change in charge carrier density or type caused by the introduction of acceptor or donor states [25]. The incorporation of Na into absorber compounds has had both positive and negative effects on solar electrical efficiency. In the case of CZTS-based solar cells, Na-doping improves electrical conductivity, and grain size, resulting in solar cell efficiency comparable to $CuInSe_2$ films. As a result, Na-doping in CZTS-based thin film solar cells has gotten a lot of coverage in the research community [26].

Lithium is required to alloy with the kesterite process, resulting in the solid solution $(Li_xCu_{1-x})_2ZnSn(SSe)_4$, which provides a method of tuning the semiconductor bandgap by increasing the Li/(Li+Cu) ratio. The lithium alloying in the CZTSSe formation process is verified by the proportional rise in lattice parameter and bandgap from 1.05 to 1.18 eV. For x up to 0.07, grain size increases, while a larger lithium fraction results in a porous absorber morphology due to an inhomogeneous distribution of Li-containing compounds in the kesterite-type materials [27].

Potassium (K) doping increases carrier density, boosts carrier collection, and passivates the front interface and grain boundaries, resulting in improved V_{oc} and J_{sc} values. K doping on CZTSSe thin film deposited by simply adding KCl into the absorber precursor solution. In [28] it was found that with K doping, the PCE of the CZTSSe system was increased from 5% to over 7% by optimizing the selenization time.

Rb doping increases the concentration of Na in the absorbers by 2.5 times, suppresses Zn aggregation at the CZTSSe/Mo interface, and eliminates the high-resistance ZnSe step, lowering the solar cell's R_s. As a result, Rb doping will boost Rb:CZTSSe solar cells' conversion efficiency to 8.41% while simultaneously increasing V_{oc}, J_{sc}, and *FF* [29].

Since cesium is one of the largest cations with an ionic radiu of 1.81 Å, replacing copper, zinc, or tin in the kesterite crystal cell would be difficult. This should result in kesterite with a high purity. Some cesium salts and mixed cesium salts have melting points between 400 and 900 degrees Celsius, which are ideal for kesterite synthesis [30]. Overall, it has been observed that cesium influences grain growth and desired orientation, as well as increasing efficiency of CZTS [31].

1.4.5 Phase diagram of CZTS

The quaternary $Cu_2ZnSn(S,Se)_4$ compound contains a large number of elements, which results in a relatively small single phase area and the creation of secondary phases, making it difficult to develop a single phase substance. Secondary phases are often harmful to the efficiency of solar cells [23].

The phase equilibrium study in the Cu_2S-ZnS-SnS_2 system revealed that single phase CZTS crystals can only be grown in a very narrow area (Figure 1.7). As a result, the synthesis of CZTS compounds without major secondary phase presence is quite challenging. The binary and ternary secondary phases such as Zn_xS, Cu_xS, Sn_xS, and Cu_xSnS_y are often observed in CZTS compounds [24].

Highly performed CZTS solar cells are slightly Zn-rich and Cu-poor [32][33]. However, secondary phases such as ZnS and Cu_2SnS_3 are readily formed in a Zn-rich regime

during thin film formation. Inhomogeneity was thought to lead to a relatively low efficiency by the inclusion of these secondary phases [24].

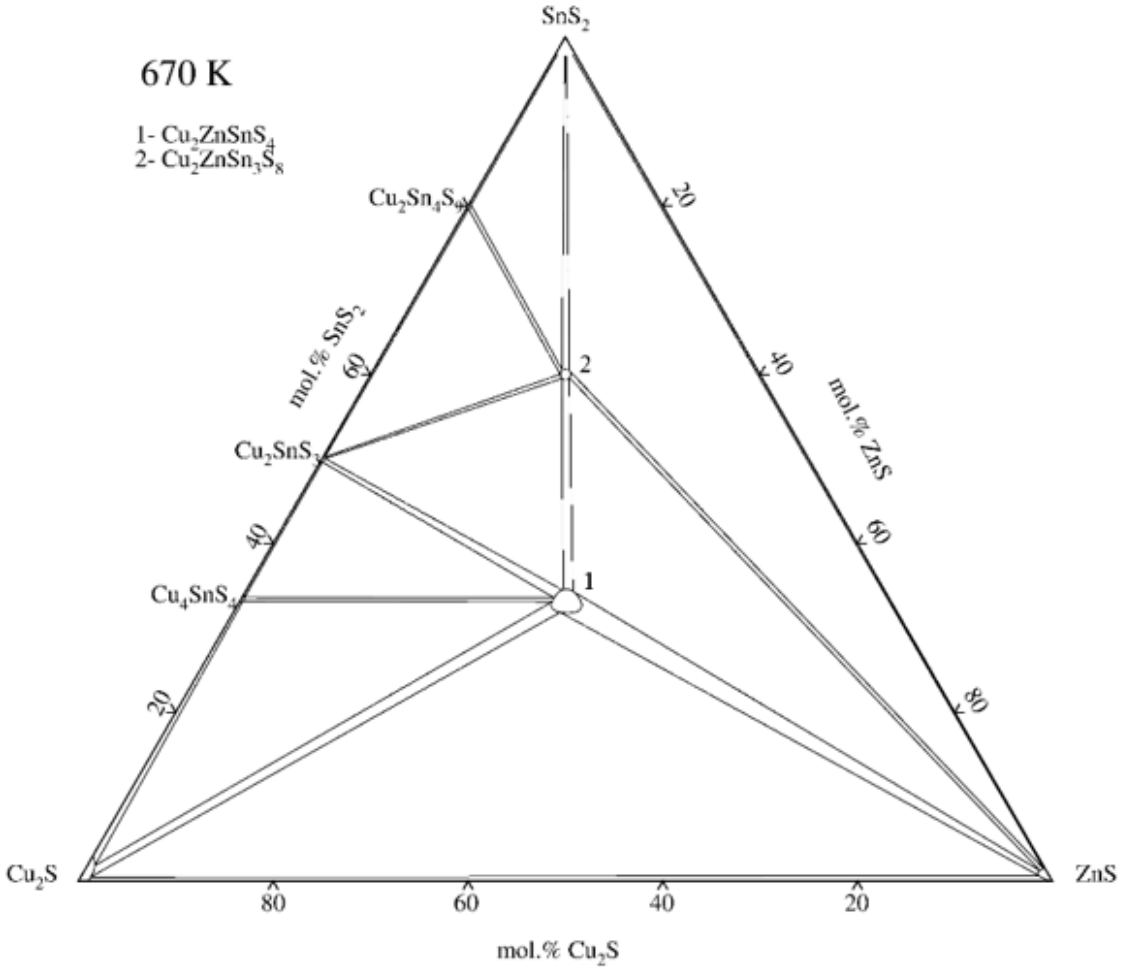

Figure 1.7 Phase Diagram of SnS-Cu_2S-ZnS solar cells [24].

It is nevertheless normal to detect secondary stages with CZTS only XRD because kesterite CZTS has several overlapping peaks with cubic ZnS and Cu_2SnS_3, which is less simple than with CIGS. Raman spectroscopy is often combined with XRD results to characterize CZTS thin films (Figure 1.8) [24].

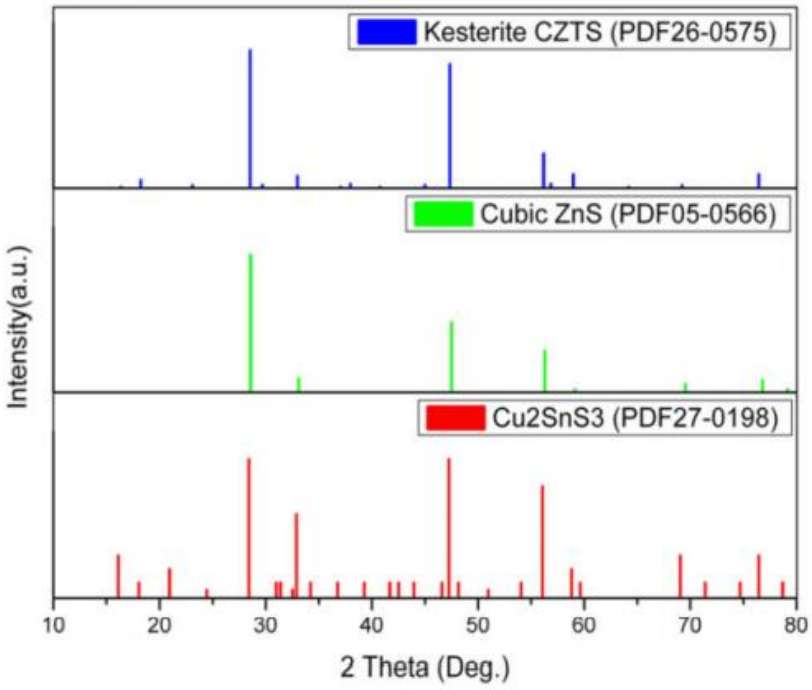

Figure 1.8 Comparison of XRD peaks of CZTS, ZnS, and Cu_2SnS_3 [24].

Owing to the limited precision of deposition rate regulation and/or the unpredictable nature of the numbers of elements and precursor stages, most current methods, including evaporation, sputtering, and ink-based techniques, it is impossible to obtain exceedingly accurate composition control [34].

1.4.6 Formation of Cu_2ZnSnS_4

Kesterites can be synthesized from pure elements, intermetallic compounds or binary sulfides. CZTS needs temperature between 500 and 600 °C to be synthesized. Metal binaries such as Cu_6Sn_5, Cu_5Zn_8, Cu_3Sn and CuZn can be formed at room temperature. Metalchalcogenide binaries such as CuS, Cu_2S and SnS can be formed between temperature ranges 200 and 450 °C. Cu_xS binaries at temperature higher than 450 °C react with Sn to form Cu_xSnS_y. Afterwards, ZnS react with Cu_2SnS_3 to form Cu_2ZnSnS_4 between temperature ranges 550 and 580 °C, it is shown in the equation below [25]:

$$Cu_2SnS_3 + ZnS \rightarrow Cu_2ZnSnS_4$$

In the research [35], the reaction pathway of CZTS compound from binary precursors were investigated. At 270 °C, Cu_2S, SnS_2, and S peaks were observed in XRD, while at 350 °C, the sample contained metallic phases of Cu_6Sn_5 and Cu_3Sn as well as binary sulfides. At 470 °C, CZTS peaks were discovered alongside ZnS, CuS, and $Cu_{2-x}S$. At 530 °C, the CZTS peak became the dominant peak, but a weak Cu_2S peak persisted in

the spectra. At 580°C the CZTS peak was clear and well identified. Raman analysis reveals that before Cu_2ZnSnS_4 is formed there were intermediate ternary phases such as Cu_2SnS_3, Cu_4SnS_4 and Cu_4SnS_6. Equation 1.1 – 1.3 indicates the principal pathways of reaction for Cu_2ZnSnS_4 formation [36].

350-400°C: $Cu_2S + SnS_2 \rightarrow Cu_2SnS_3$ 1.1

350-700°C: $Cu_2S + SnS_2 + ZnS \rightarrow Cu_2ZnSnS_4$ 1.2

350-700°C: $Cu_2SnS_3 + ZnS \rightarrow Cu_2ZnSnS_4$ 1.3

Muska *et al.* reported that the elemental composition of the precursors used for synthesis influence the final composition of the CZTS monograin powder grown in KI [37]. Several reports have shown that growing absorber materials in Cu-poor/Zn-rich conditions results in the highest solar cell efficiencies [38][39][40].

1.4.7 Review of CZTS preparation techniques

The performance of CZTSSe solar cells is closely related to the stoichiometry and crystallization quality of CZTSSe absorber layers. To achieve the requisite stoichiometry and crystallinity, it is important to understand the growth mechanism of kesterite solar cell absorber materials. CZTS has a rather small stoichiometric single-phase area. Secondary phases in the absorber layers, such as ZnS, SnS, Cu_2SnS_3, and CuS, form very easily under Cu-poor and Zn-rich conditions. As a result, the synthesis of non-impurity stoichiometric single-phase CZTS films is difficult. The existence of secondary phases is related to the low efficiency of CZTS solar cells. As a result, it is important to use the proper raw materials and preparation methods in order to achieve highly effective CZTS solar cells [17].

In 1988 [41], Ito and Nakazawa discovered the photovoltaic effect in a heterodiode consisting of a cadmium-tin-oxide clear conductive film and a CZTS thin film on a stainless-steel substrate with a V_{oc} of 165 mV. In 1989, they obtained an open-circuit voltage of 250 mV and a short-circuit current of 0.1 mA/cm^2 by annealing the same experiment in air. In 1997, Friedlmeier *et al*. produced in high vacuum CZTS thin films by thermal evaporation of elements and binary chalcogenides [41]. All sputtering methods have several similarities, the most notable of which is the use of physical processes such as laser ablation or the use of energetic particles to separate material from a target material and inject it in the vapor state of a substrate. In comparison to the chemical vapour deposition, the precursor gas containing the material to be deposited is reacted in the chamber and deposited onto the substrate [42]. Non-vacuum approaches using nano particles inks is another promosing approach. This technique

has the advantage of being easily adaptable for large-scale manufacturing; it consists primarily of ink formulation, inkjet printing, and annealing [43][44]. Hydrazine-based solution-particle slurry, electrodeposition, and spray pyrolysis are all notable approaches [16]. Wibowo *et al.* demonstrated a simple technique for synthesizing single phase $Cu_2ZnSnSe_4$ powders at 500 °C in a quartz tube furnace under an Ar flow at atmospheric pressure using a solid-state reaction from elemental Cu, Zn, Sn, and Se powders. Such non-vacuum thin-film fabrication methods offer cost savings, but reproducibility and film quality are impaired. The synthesis of CZTSSe from initial binary compounds in isothermal re-crystallization in different molten fluxes has been demonstrated using powder technologies, which are among the most cost-effective materials processing methods [45].

1.5 Monograin powder technology

1.5.1 Overview of the monograin powder technology

Solar panels are currently manufactured mostly using wafers and thin film methods. Unfortunately, this is a very expensive process in terms of both financial and energy resources. The idea of making solar cells out of powder materials is about as old as the existing silicon-based solar cells. However, monograin powder crystals replace monocrystalline wafers or thin films in monograin layer solar cells, allowing for less costly and more efficient material processing and material loss [46]. Monograin powder crystals are embedded in an organic resin to create the monograin layer (MGL). The monograin layer (MGL) incorporates the advantages of polycrystalline materials with the best photoelectrical properties of single crystals, such as low cost and basic material and layer preparation technology, and the ability to create devices with virtually unlimited area [38]. The key advantage of monograin layer (MGL) technology is that the fabrication of absorber/junction forming, and cell/module formation are isolated, resulting in many advantages in both stages of MGL development. High temperatures are used only in the manufacture of absorber materials, and the use of affordable, durable, low-temperature substrates for membraine making enables the manufacture of inexpensive flexible solar cells [46].

1.5.2 Monograin powder growth

Isothermal recrystallization of II-VI polycrystalline powders in the presence of a suitable flux material liquid phase in an amount sufficient to repel initial crystallites results in the formation of semiconductor compounds with single-crystalline grain structure and narrow-disperse granularity, known as monograin powders [47][48]. The formation of monograin powders through isothermal recrystallization of initial powders in various fluxes have been described in [49][50][51][52]. Constituent elements, binary chalcogenides, elemental metal alloys, and chalcogenides are used as precursors to prepare quaternary compounds. The liquid phase of a flux material is useful for multi-component compound synthesis as it enables rapid diffusion of constituent elements through the liquid phase, resulting in a uniform composition of absorber materials for solar cells [53]. The variation in surface energies of crystals of different sizes turns out to be the driving force in the monograin powder growth. The previous reports have shown that the growth of single crystalline powder grains takes place at temperatures above the melting point of the used flux material [54]. The composition of the flux and recrystallization temperature determine the equilibrium conditions in a closed isotheraml system as well as the properties of the produced powder crystals.

1.5.3 Flux materials

A dissolving agent for absorber material, named as a flux material, is used in monograin technology [40]. In general, they are made up of oppositely charged species, but the nature of these species varies, ranging from classical ions in molten salts to charged polyatomic molecules in ionic liquids. Fused alkali halides, which include closed-shell alkali and halogen ions, are the prototype of molten salts The requirements to the flux material are chemical stability, readily available, inexpensive and easily removable (soluble in water) allowing the powder particles to be quickly removed from the flux [54]. It is preferable to have a medium melting temperature and a low vapor pressure at the heating temperature. [55]. In the monograin powder technology several flux materials, including NaI, KI, $SnCl_2$ and CdI_2 have been studied [48] [56] [57]. It was found that the used molten salts could react with the used precursors or get incorporated into the final products. Therefore, it is very important to study the effect of flux material to the produced powder properties. In this study, the usage of CsI, RbI, LiI and NaI as flux material for the synthesis of Cu_2ZnSnS_4 monograin powders and the influence on the powder crystals properties is presented for the first time.

Sodium iodide (NaI) molar mass is 149.89 g/mol. Sodium Iodide (NaI) is an ionic compound that contains sodium cation (Na^+) and iodide anion (I^-). It comes in the form of odorless white crystals or powder with density of 3.67 g/cm3, melting point of 651 °C and boiling point of 1304 °C. Its solubility in the water at 25 °C is 1842 g/L. It's a deliquescent solid that absorbs moisture. In water and certain organic solvents, sodium iodide is highly soluble. It is sensible for air, humidity, sun, and solid NaI, due to the production of iodine gases, turns brown when exposed to air or light. Even strong oxidants, strong acids and bromine trihalides produce iodine and react violently [58].

Lithium iodide (LiI) is an inorganic compound of product lithium and iodine. Its molar mass is 133.85 g/mol. Reaction with air can be quickly detected because iodine formation by iodine oxidation transforms white to yellow. Lithium iodide can be found in many different types of hydrates, including monohydrate, dehydrate, and trihydrate. It is adequately soluble in ammonium hydroxide, and it can be dissolve in water, alcohol, acetone, and methanol. It melts at 469 °C and its boiling point is at 1170 °C. In the water the solubility rate at 25 °C is 1670g/L [59].

Cesium Iodide (CsI) is generally easily accessible. Though, for producing iodide solutions, iodide-rich solutions act as better dissolving agents. Its molar mass is 259.81 g/mol. CsI is white crystalline in appearance with a density of 4.5 g/cm^3, melting point of 626 °C and boiling point of 1277 °C. Its solubility in water at 25°C is 848 g/L [60].

Rubidium Iodide (RbI) is in most cases readily available. Usually, it is stable but may be sensitive to light and air. Rubidium iodide is a salt with a melting point of 642 °C. Its molar mass is 212.372 g/mol. Its melting point is 642 °C. Density of RbI is 3.55 g/cm^3. Rubidium iodide is a colorless crystal that is water soluble, 1520 g/L at 25 °C. It has a flame that is red violet in colour [61] [62].

Potassium Iodide (KI) is a potassium and iodide metal halide that protects against thyroid and expectorants. The odorless white solid is potassium iodide. Lowering and blending with water. It is a scavenger of hydroxyl radicals. Its molar mass is 166.003 g/mol. The melting point of KI is 681 °C. It is slightly soluble in ethanol and the solubility in water at 25 °C is 1428 g/L [63].

1.6 Summary of literature overview and the aim of the study

The sun is an inexhaustible supply of free energy for the planet Earth. New technologies are currently being used to produce electricity from collected solar energy. These methods have already been proven and are commonly used as sustainable alternatives to traditional non-hydro technologies around the world. Silicon wafers, which are known to be expensive, currently dominate the PV market. Thin films, on the other hand, despite having a reasonable conversion efficiency and optical properties, are unable to meet the necessary energy demand because indium, gallium, and tellurium reserves are limited and costly. A focus in creating a renewable technology is the production of non-toxic solar panel materials manufactured from easily available elements rather than rare and precious metals. The kesterite structure semiconductors $Cu_2ZnSn(S,Se)_4$ are one of the potential candidates as a light absorber medium to lead the next generation of thin film solar cells due to its low cost, non-toxic, and plentiful source of materials.

Monograin layer-based technology has many advantages like the separation of materials formation from the module fabrication allowing for all temperatures and purity precautions. In monograin layer solar cells monograin powders are used as absorber materials that replace wafers or thin films in photovoltaic device. Monograin powders are produced by synthesis-growth method in molten salt media (liquid phase of flux material). Monograin powder technology allows for cheaper and much more efficient materials production and minimize materials loss.

In the monograin powder technology several flux materials, including NaI, KI, $SnCl_2$ and CdI_2 have been studied. It was found that the used molten salts could react with the used precursors or get incorporated into the final products. Therefore, it is very important to study the effect of flux material to the produced powder properties. In this study, the usage of CsI, RbI, LiI and NaI as flux material for the synthesis of Cu_2ZnSnS_4 monograin powders and the influence to the powder crystals properties is presented for the first time. Moreover, as various alkaline metals have shown a positive effect on thin film solar cell parameters, one aim of this research is to find out how the powder growth in one or another alkaline salt impact the performance of monograin layer (MGL) solar cells.

2 EXPERIMENTAL

In this study CZTS monograin powder materials were synthesized from binary chalcogenides and elemental sulfur in the liquid phase of different flux materials (CsI, RbI, LiI, NaI and KI). The synthesis-growth process of CZTS monograin powders were performed in evacuated quartz ampoules at 740 °C for 136 hours.

Table 2.1 shows main properties of Cu_2ZnSnS_4 and flux materials which have been used in this experimental research.

Tabel 2.1. Properties of CZTS and flux materials.

Molecular Formula	Molar Mass (g/mol)	Density (g/cm^3)	Melting Temperature (°C)	Water Solubility at 25°C (g/L)	Ionic radii of alkali metals (Å)
CZTS	439.47	4.56	990	Not soluble	-
NaI	149.89	3.67	651	1842	102
LiI	133.85	4.08	469	1670	76
CsI	259	4.50	626	848	167
RbI	212.3	3.55	642	1520	152
KI	166	3.12	681	1480	138

2.1 Preparation of CZTS monograin powders

Five Cu_2ZnSnS_4 powder materials were synthesized from binary compounds CuS (5N), ZnS (5N), SnS (5N) and elemental sulfur (5N) by isothermal synthesis-growth method in five different molten salts (flux materials): cesium iodide (CsI), rubidium iodide (RbI), lithium iodide (LiI), sodium iodide (NaI) and potassium iodide (KI).

The used precursor compounds CuS and SnS were self-synthesized from high purity Cu and Sn shots (5N, Alfa Aesar), respectively and sulfur pieces in evacuated quartz ampoules by Dr. Jaan Raudoja in TalTech Laboratory, ZnS (5N) and elemental sulfur (5N) were commercially available.

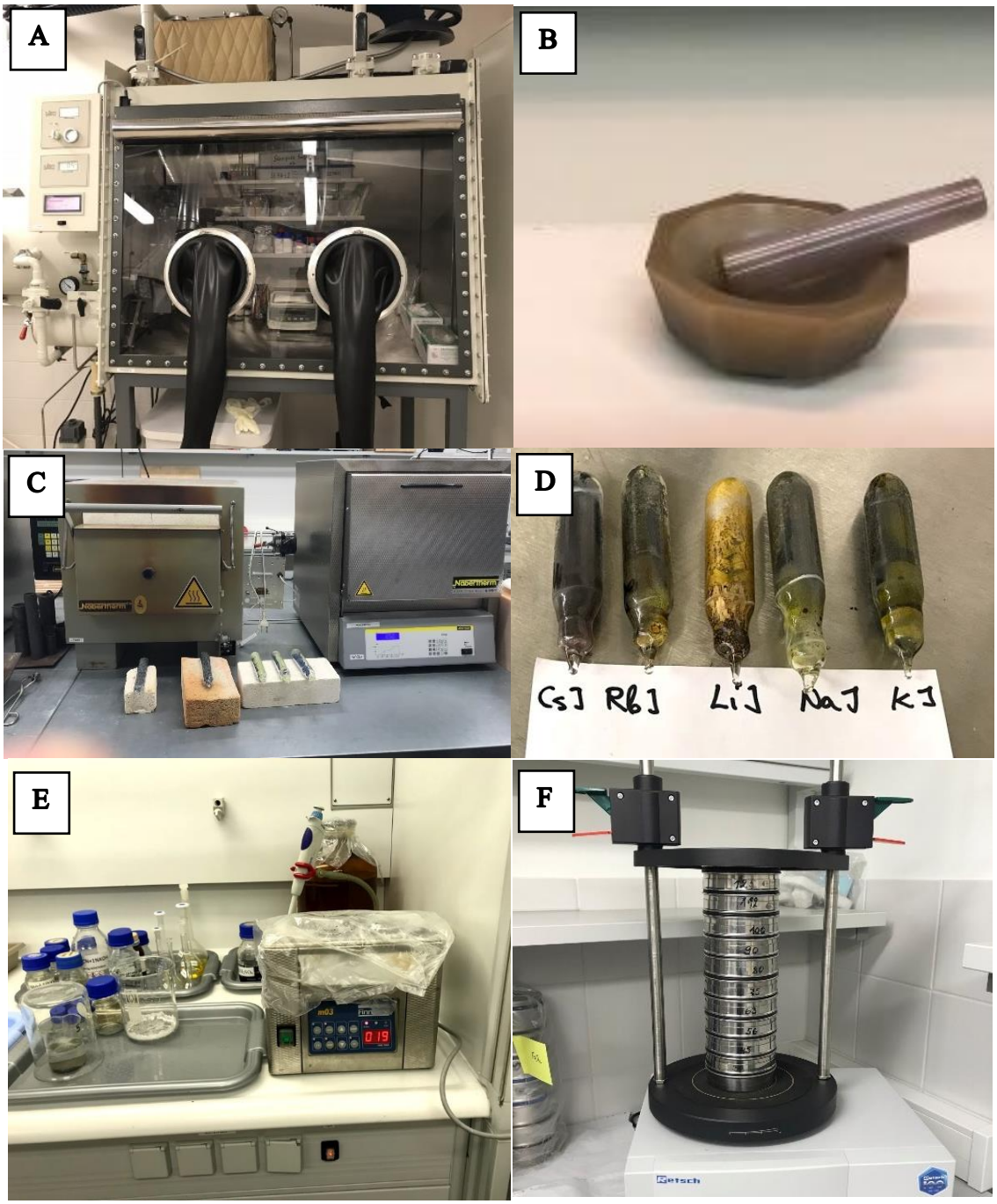

Figure 2.1 Experimental steps of the monograin powder preparation process: (A) glove box filled with Argon gas, (B) the precursors were mixed manually in agate mortar to ensure homogeneous mixture, (C) chamber furnace used for annealing, (D) annealed samples with different flux materials showing their different colors and appearances, (E) ultrasonic bath used during washing process to remove flux material, (F) the sieving machine containing sieves with different mesh widths (ranging from 38μm to 112 μm).

The preparation of the five samples were conducted in a glove box (Figure 2.1 A), because of the hydroscopic nature of some fluxes (LiI and NaI) that makes the syntheses process complicated. Precursors were initially weighed for the composition of $Cu_{1.85}Zn_{1.1}SnS_{3.95}$ and 4.45% of mole excess of S stoichiometric ratios. The initial composition of CZTS was selected based on our research group previous experiments and as the best solar cell results have achieved using this chemical composition.

The volume ratio of solid precursors for CZTS to the flux salt was kept constant $V_{CZTS}/V_{flux}(cm^3/cm^3) = 1$ because it is significant in monograin powder technology to deliver enough volume of the liquid phase between the solid compound particles. The weighed precursors were grinded in an agate mortar (Figure 2.1 B) to improve the homogeneity and loaded into quartz ampoules. The mixtures in ampoules were degassed under dynamic vacuum at 100 °C and sealed. The annealing process of the materials was carried out in the chamber furnace (Figure 2.1 C) at 740 °C for 136 hours. The growth processes were stopped by taking the synthesis ampoules out from the furnace to room temperature after the synthesis duration was reached (Figure 2.1 D).

The synthesized powder particles were released from flux salt by leaching and rinsing with distilled water (Figure 2.1 E). During the washing process ultrasonic bath was used for shaking. The ultrasonic bath water was heated up to 50°C to increase the flux material solubility speed in washing water. This process was repeated several times until a completely clear washing water was obtained indicating that all the flux material has been completely removed. After the removal of flux, the obtained monograin powders were dried in a furnace at 50 °C for over-night and sieved into narrow size granulometric fractions (38 to 112 μm) by sieving system Retsch AS 200 (Figure 2.1 F).

2.2 Preparation of CZTS monograin layer solar cells

The obtained CZTS monograin powder crystals grown in different molten salts, were used as absorber material in monograin layer (MGL) solar cells with the following structure: graphite/CZTS/CdS/i-ZnO/ZnO:Al/Ag/glass. The required p-n junction was formed by depositing an *n*-type CdS buffer layer on the *p*-type CZTS crystals using the chemical bath deposition method. Halfway into the epoxy coat, a monolayer of approximately uniform-size CdS-covered powder crystals was added for making the monograin layer membranes. After polymerization of the epoxy, on the top of the membranes, a window layer of ZnO (i-ZnO and contactive ZnO:Al) was deposited by radio frequency magnetron sputtering. A silver paste was added to the ZnO window layer to create the front collector, and the structure was then adhered to a glass substrate with epoxy glue. Afterwards, the supporting plastic foil from the structure was

removed, with the help of concentrated H_2SO_4. The etching prcoess was carried out to partly release the surfaces of powder crystals at the back contact side. As a last step, a mechanical abrasive treatment was applied to the opened surface side of powder crystals. A conductive graphite paste was used as back contacts [55][64][52]. A schematic structure of monograin layer solar cell is shown in Figure 2.2. Monograin layer solar cell membranes were prepared by Dr Maris Pilvet.

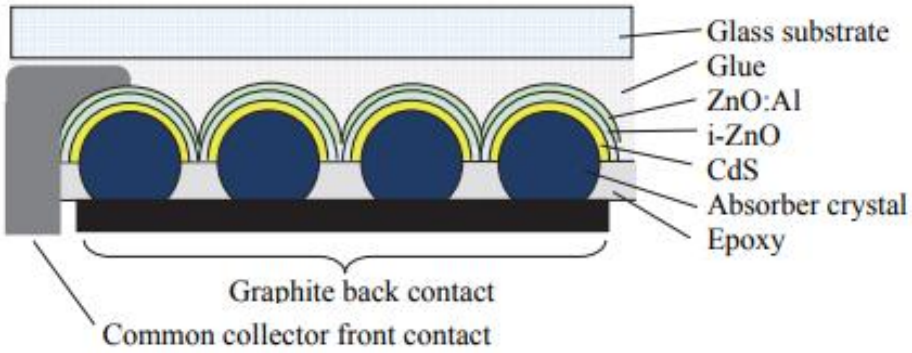

Figure 2.2 Schematic of monograin layer solar cell [65].

2.3 Characterization of monograin powders and solar cells

2.3.1 Scanning electron microscopy (SEM)

The scanning electron microscope (SEM) is one of the most powerful tools to analyze the microstructure morphology [66]. SEM generates a range of signals at the surface of solid specimens by using a directed beam of high-energy electrons. The signals generated by electron-sample interactions reveal details about the sample such as its exterior morphology (texture), the crystalline structure and orientation of the materials that comprise the sample. In most applications, data are obtained over a specific region of the sample's surface, and a 2-dimensional image displaying spatial variations in these properties is created.

Using conventional SEM techniques, areas varying in width from 1 cm to 5 microns can be imaged in a scanning mode (magnification ranging from 20 x to approximately 30 000 x, spatial resolution of 50 to 100 nm)[67]. The morphology of synthesized powder crystals was studied using a Zeiss ULTRA 55 high-resolution scanning electron microscope (HR-SEM). The SEM photos were created by Dr. Valdek Mikli in Tallinn University of Technology.

2.3.2 Energy dispersive x-ray spectroscopy (EDX)

Energy dispersive X-ray analysis, or EDX analysis, is also known as energy dispersive X-ray microanalysis. It is an analytical method to determine a sample elemental composition or chemical characterization. It is based on an association between an X-ray source and a sample. Its characterization abilities are largely due to the underlying assumption that each element has a special atomic structure, resulting in a unique range of peaks on the X-ray emission spectrum [68]. A Bruker Esprit 1.8 EDX system (the measurement error is about 0.5 at. %) was used to investigate the elemental composition of the monograin powders. The EDX measurements were carried out by Dr. Valdek Mikli in Tallinn University of Technology.

2.3.3 Raman spectroscopy

Raman scattering is one of the most popular spectroscopies used to detect vibrations in molecules. Raman spectroscopy is commonly used to provide knowledge on chemical structures and physical shapes, to distinguish compounds based on their distinctive spectral patterns (‘fingerprinting') and to determine the quantity of a substance in a sample quantitatively or semi-quantitatively [69].

Its substance analysis is focused on the interaction of laser light with chemical bonds in the material. As light interacts with molecules in a gas, solid, or liquid, most of the photons diffuse or scatter at the same energy level as incident photons. This is known as Rayleigh scattering or elastic scattering. About one photon out of every ten million will be dispersed at a frequency different from the incident photon. A material's chemical composition, phase analysis, intrinsic stress/strain contamination, and impurity can all be determined using Raman Spectroscopy [70]. In this study, the phase structure and inclusion of secondary phases were investigated at room temperature by using Horiba's LabRam HR800 spectrometer with a configuration of 532 nm laser line, filter D1 and measured with in 100 seconds.

2.3.4 X-ray diffraction analysis (XRD)

X-ray powder diffraction is a fast-analytical technique mainly used to identify crystalline material in a phase and can provide unit cell dimensional detail. The substance studied is finely ground, homogenized and is measured by average volume composition [71]. The powder X-ray diffraction (XRD) patterns were recorded using a Rigaku Ultima IV diffractometer with Cu K_α radiation (λ = 1.5406 Å) at 40 kV and 40 mA operating with the silicon strip detector D/teX Ultra. The XRD measurements of all samples were carried out by Dr. Rainer Traksmaa.

2.3.5 Solar cell characterization

The MGL solar cells were characterized by measuring the *J–V* characteristics with a Keithley 2400 source meter under standard test conditions (AM 1.5, 100 mW cm^{-2}) obtained using a Newport solar simulator. Due the epoxy between crystals in the monograin layer solar cell, the working area is approximately 75% of the total area. Therefore, the MGL solar cell efficiency values were re-computed for the active area (η_{active}). The main parameters used to characterize the performance of MGL solar cells were short-circuit current density (J_{sc}), open circuit voltage (V_{oc}), fill factor (*FF*) and the solar energy conversion efficiency (η).

The fill factor of the solar cell is the ratio of the maximum power ($P_{max} = J_{mpp} \times V_{mpp}$) provided by a solar cell to the product of V_{oc} and J_{sc}. The fill factor can be used to describe the quality of the solar cell junction and can be given by following equation:

$$FF = \frac{J_{mpp} \times V_{mpp}}{J_{sc} \times V_{oc}} \qquad (2.1)$$

where *FF* - fill factor;

J_{mpp} - current density at maximum power output;

V_{mpp} - voltage at maximum power output;

V_{oc} - open circuit voltage;

J_{sc} - short circuit current density.

The solar cell conversion efficiency is calculated as the ratio between the maximum generated power and the incident power (the power density from the reference light source) [72]. The efficiency can be given by following equation:

$$\eta = \frac{J_{sc} \times V_{oc} \times FF}{P_{in}} \quad (2.2)$$

where η - efficiency;

J_{sc} - short circuit current density;

V_{oc} - open circuit voltage;

FF - fill factor;

P_{in} - power of the standard illumination (100 mW/cm^2) used.

2.3.6 Quantum efficiency measurements

The ratio of the numbers of electrons emitted in an external circuit by an incident photon of a given wavelength can be described as the quantum efficiency of a solar cell [73]. Therefore, the effective band gap energy (Eg*) of samples were predicted through quantum efficiency measurements. Spectral response measurements were performed in the spectral region of 350-1100 nm using a computer-controlled SPM-2 prism monochromator. The generated photocurrent was detected at 0 V bias voltage at RT by using a 250 W halogen lamp. The EQE measurements were carried out with the assistance of Dr. Mati Danilson.

3 RESULTS AND DISCUSSIONS

3.1 Morphology of Cu_2ZnSnS_4 monograin powders

Figure 3.1 (A-J) shows SEM micrographs of as-grown CZTS monograin powders grown in CsI, RbI, LiI, NaI and KI molten salts. A significant difference in the size and morphology of particles grown in different molten salts is clearly seen. CZTS powder particles grown in CsI molten salt resulted in uniform and non-aggregated crystals with smooth facets and roundy edges (see Figure 3.1 A, B). The crystals grown in RbI flux resulted in crystals with uneven edges, irregularities of porous surface and shape as presented in Figure 3.1 C, D. Whereas in the case of LiI, the powder contain well-formed individual crystals. The crystal shapes are uniformly roundy with rounded however porous edges (see Figure 3.1 E, F). When it comes to crystal growth, a round shape body is preferable because it has less surface energy than a tetragonal shape. Furthermore, the round form of crystals means the precursors are more soluble and/or formed compound (CZTS) in LiI than in other used flux materials. Figure 3.1 G, H shows SEM micrographs of CZTS powder crystals grown in NaI. The powder consists of non-aggregated and sintered crystals. The well-formed individual crystals have flat and smooth facets with sharp edges. This result specifies the slow solubility of CZTS in the liquid phase of NaI. The coexistence of sintered and non-aggregated crystals shows that parallel processes: At the same time, monograin development in the molten phase and the sintering process are taking place. The growth of CZTS in KI molten salt (see Figure 3.1 I, J) resulted in different and uneven shape of crystals. Mainly agglomerated crystals with rough and porous edges can be seen.

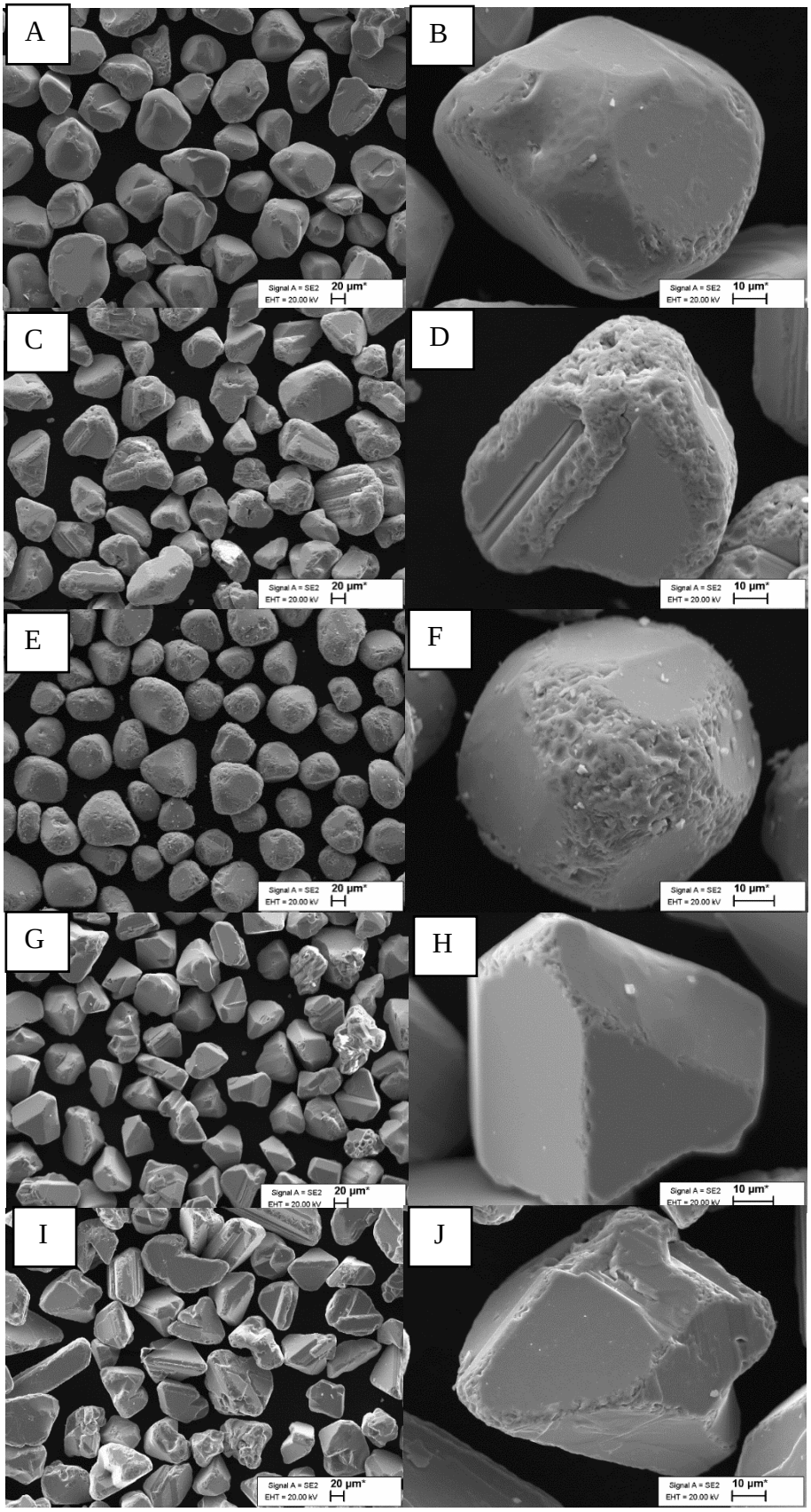

Figure 3.1 SEM images of Cu_2ZnSnS_4 monograin powder crystals grown in CsI (A, B), RbI (C, D), LiI (E, F), NaI (G, H) and KI (I, J) molten salts.

3.2 Compositional analysis of CZTS monograin powders

The EDX results of the average concentration ratio values of Cu/(Zn+Sn), Zn/Sn and S/Metals of the synthezised CZTS monograin powders are presented in Table 3.1. The EDX analysis is compiled on at least 8 different polished grains for each of the synthesis in different flux materials. Figure 3.2 illustrates the elemental concentration ratios of the input and the resuted CZTS synthesized in five different flux materials. This gives an overview of how the respective outcome chemical composition of CZTS changes by using different flux materials i.e. CsI, RbI, LiI, NaI and KI. Variations have been observed between the input composition ($Cu_{1.85}Zn_{1.1}SnS_{3.95}$) and the obtained composition of CZTS monograin powders synthesized in different molten salts. Furthermore, the deviation ranges from one flux material to the next.

Tabel 3.1 Concentration ratios of Cu/(Zn+Sn), Zn/Sn, S/Metals and final composition of Cu_2ZnSnS_4 synthesized in different flux materials (CsI, RbI, LiI, NaI and KI) according to EDX analysis.

Flux Material	Cu/(Zn+Sn)	Zn/Sn	S/Metals	Final composition
CsI	0.97	1.01	1.00	$Cu_{1.97}Zn_{1.02}Sn_{1.01}S_4$
RbI	0.91	1.06	1.00	$Cu_{1.90}Zn_{1.07}Sn_{1.01}S_4$
LiI	0.87	1.02	1.05	$Cu_{1.77}Zn_{1.03}Sn_{1.01}S_4$
NaI	0.92	1.03	1.01	$Cu_{1.90}Zn_{1.04}Sn_{1.01}S_4$
KI	0.92	1.04	1.01	$Cu_{1.90}Zn_{1.05}Sn_{1.01}S_4$

In input composition of CZTS the elemental ratios were: Cu/(Zn+Sn) = 0.88, Zn/Sn=1.1 and S/Metal=1.0 (Table 3.1). A copper poor and zinc rich composition of CZTS was obtained by using RbI, LiI, NaI or KI as flux material. Although, in the case of all powders the ratio of Zn/Sn (varied from 1.01 to 1.06) was lower than the input ratio of 1.1. The highest Zn/Sn ratio (1.06) was measured from the CZTS monograin powder grown in RbI. The decrease in Zn content in the final powder composition is most likely a result of some unreacted ZnS precursor that was detected by EDX from polished cross-section of crystals (see Figure 3.3). In the case of CsI the produced monograin powder showed nearly stoichiometric chemical composition (Cu/(Zn+Sn) = 0.97, Zn/Sn = 1.01 and S/Metals =1.0). In the case of CZTS powder synthesized in LiI, the ratio of Cu/Zn+Sn = 0.87 is even lower than the used input ratio of Cu/(Zn+Sn) = 0.88, and much lower compared to the other materials (varied from 0.91 to 0.97). Also, Zn/Sn ratio decreases in the LiI obtained material as compared to the powders grown in RbI, NaI and KI molten

salts. The variations in the S/Metals ratios are not so great except in the case of lithium iodide, it increased.

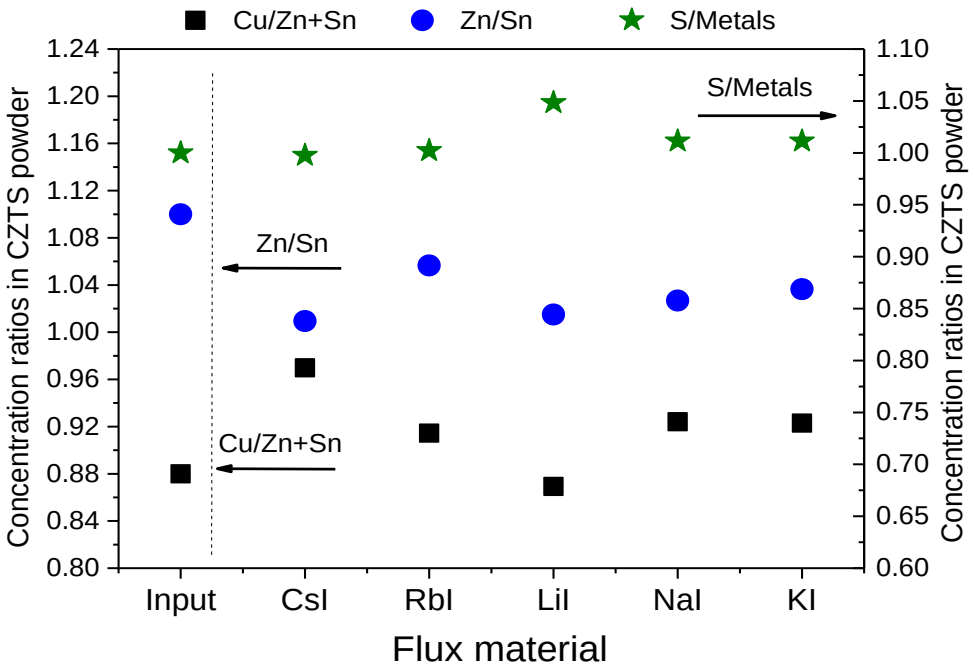

Figure 3.2 The concentration ratios of Cu/(Zn+Sn), Zn/Sn and S/Metals of monograin powders synthesized in different molten salts.

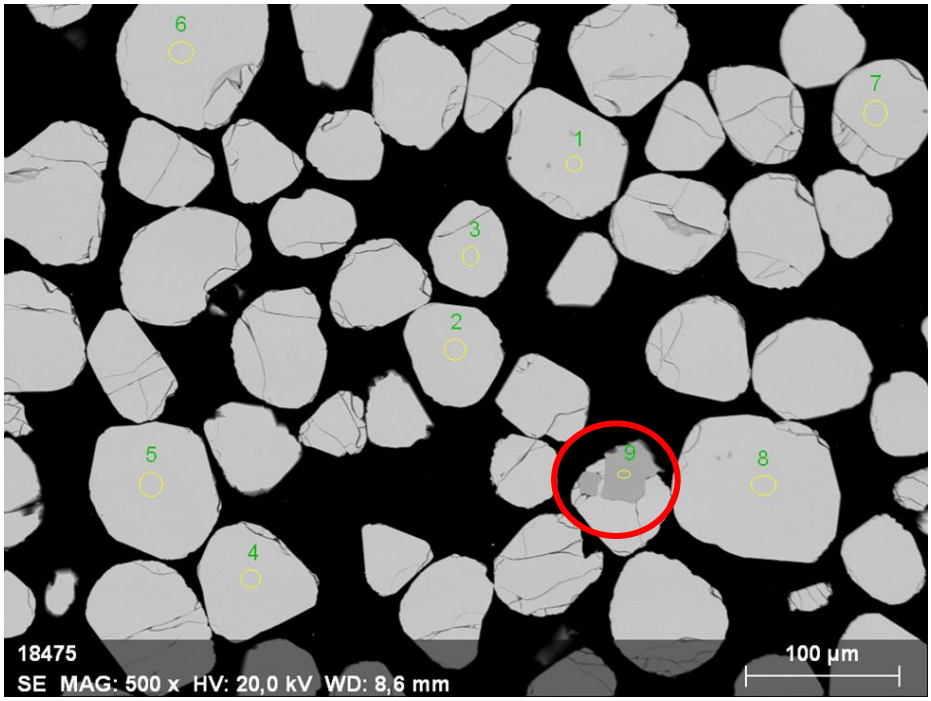

Figure 3.3 SEM image of polished cross-section of CZTS monograin powder synthesized in LiI molten salt. The highlighted red circle indicates darker gray areas, signifying secondary phase of ZnS.

3.3 Phase composition of the Cu_2ZnSnS_4 monograin powders

3.3.1 X-ray powder diffraction

XRD analysis was applied to characterize the phase purity and the crystal structure of the synthesized Cu_2ZnSnS_4 monograin powders. XRD patterns of the Cu_2ZnSnS_4 monograin powders grown in five different flux materials are shown in Figure 3.4 a. All the diffraction peaks including the major peaks (101), (112), (220) and (312) could be indexed according to a tetragonal kesterite type phase structure. No secondary phases were detected. XRD pattern of CZTS MGPs grown in LiI (red line) reveals shift of the diffraction peaks towards lower angles. Figure 3.4 b illustrates the enlarged view of the (112) lattice plane diffraction peak shift from 28.45 to 28.40° for powder grown in LiI. Furthemore, the crystals grown in LiI have bigger lattice parameters (*a*, *b* and *c*) values in comparison with those powders formed in CsI, RbI, NaI and KI (see Figure 3.5). This kind of behaviour indicates to the incorporation of Li into the CZTS compound from the molten salt of LiI. Most probably, the Li^+ (0.76 Å) ions replaced partly the Cu^+ (0.74 Å) ions causing the expansion in the lattice. All the XRD analysis results are in good correlation with the results published in literature [74].

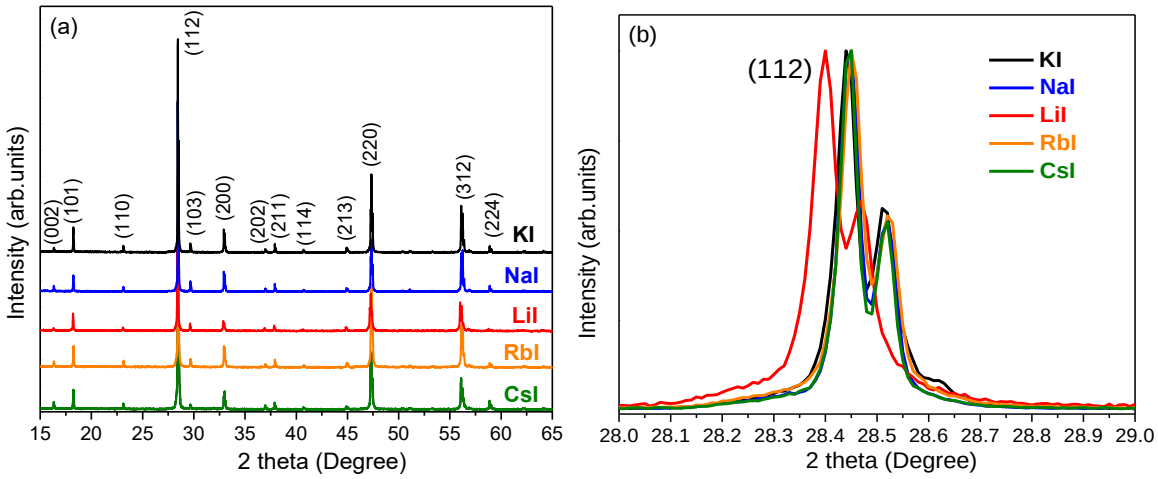

Figure 3.4 (a) X-ray diffraction patterns of the Cu_2ZnSnS_4 monograin powders grown in CsI, RbI, LiI, NaI and KI molten salts, (b) the enlarged view of the (112) diffraction peaks.

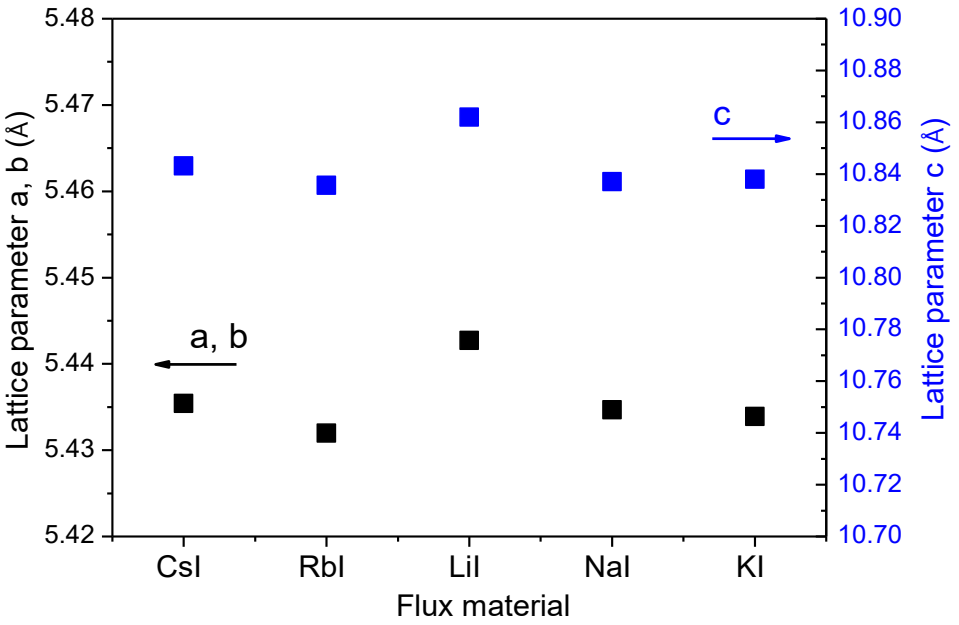

Figure 3.5 Lattice parameters *a*, *b* and *c* of Cu_2ZnSnS_4 monograin powders grown in CsI, RbI, LiI, NaI and KI molten salts.

3.3.2 Raman spectroscopy

Raman spectroscopy investigations were used to identify the secondary phases that cannot be differentiate by XRD due to the overlapping of XRD patterns.

Figure 3.6 a illustrates the characteristics Raman frequencies of Cu_2ZnSnS_4 monograin powder grown in cesium iodide. The main A1 Raman mode at 338 cm^{-1} with a hwhm = 2.25 cm^{-1} is detected. The other CZTS Raman peaks are observed at 97, 139, 166, 250, 288, 347 and 367 cm^{-1}. These Raman peaks are characteristic to CZTS according to reference [75][76]. In addition, in the Raman spectra of CZTS monograin powder grown in CsI, the presence of ZnS phase (351 cm^{-1} [77]) is observed.

The Raman frequencies of Cu_2ZnSnS_4 monograin powder grown in RbI are shown in Figure 3.6 b. The A1 Raman mode is detected at 338 cm^{-1} with a wider hwhm = 2.81 cm^{-1} compared to the one grown in CsI. The other weaker CZTS Raman peaks are observed at 92, 166, 269, 288, 371 and 376 cm^{-1}. All these peaks belong to the CZTS according to reference [78].

For Cu_2ZnSnS_4 monograin powder grown in LiI, Raman modes are detected at 92, 165, 246, 286, 338 cm^{-1}, 371 and 377, as presented in Figure 3.6 c. The hwhm of the main Raman peak at 338 cm^{-1} is the widest in this series, 3.53 cm^{-1}. This finding is in a good agreement with the results of XRD analysis and prove once more the incorporation of Li into the CZTS lattice structure. These peaks belong to the CZTS [75].

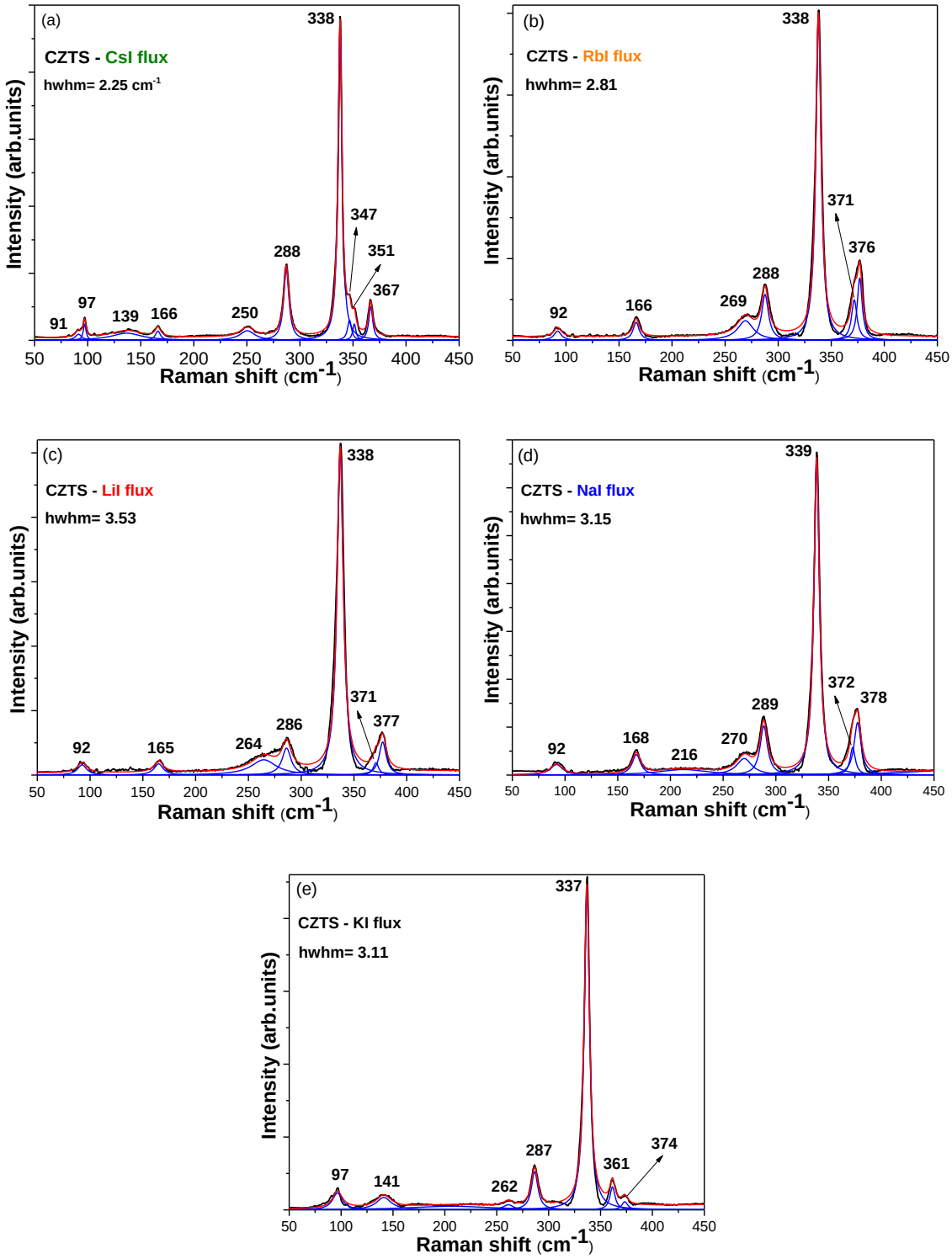

Figure 3.6 Raman spectra of Cu_2ZnSnS_4 monograin powder grown in (a) CsI, (b) RbI, (c) LiI, (d) NaI and (e) KI molten salts.

The Raman frequecnies of Cu_2ZnSnS_4 monograin powders grown in NaI are shown in Figure 3.6 d. The CZTS Raman peaks are observed at 92, 168, 270, 289, 339, 372 and 378 cm^{-1}. The A1 Raman mode at 339 cm^{-1} has a hwhm of 3.15 cm^{-1}. These peaks belong to the CZTS according to reference [75][76].

The Raman frequecnies of Cu_2ZnSnS_4 monograin powder grown in KI are shown in Figure 3.6 e. The A1 Raman mode is at 337 cm^{-1} with a hwhm of 3.11 cm^{-1}. All detected Raman peaks at 97, 141, 262, 282, 287, 337, 361 and 374 cm^{-1} correspond to the CZTS phase [37].

Raman spectroscopy was used to analyse the phase composition of Cu_2ZnSnS_4 monograin powders grown in different flux materials (CsI, RbI, LiI, NaI and KI). In all the five analysed samples, in addition to the weak peaks, the sharp characteristic peak of CZTS phase was detected in the range of 337-339 cm^{-1}. All the observed peaks match well with the reported Raman peaks in [37] [75]. A trace of ZnS, peak at 351 cm^{-1} [37] was detected in the CZTS MGPs grown in CsI. The hwhm of the main peak was varying by varying the molten salt. The width of this peak gives a hint about the reflection of the crystallinity and structural distribution. That means, the crystalline material is characterized by a sharp and a narrow Raman peak compared to the amorphous material. In our case, the CZTS MGPs grown in LiI showed the widest mode of the main Raman peak (hwhm = 3.55 cm-^{1}). This finding supports the XRD results and prove the incorporation of Li from LiI into the lattice structure. In case of CsI and RbI Raman peaks are sharp and narrow with half width of 2.25 and 2.81 cm-1, respectively, means providing a high level of crystallinity.

3.4 Device characterization

3.4.1 *I-V* curve characteristics of solar cells

All Cu_2ZnSnS_4 monograin powders synthesized in five different flux materials were used as absorber materials (*p*-type) in MGL solar cells. Prior to that, the as-grown powders were post-treated by chemical etching and annealing in a sulphur atmosphere to enhance the crystallinity of the powders, eliminate secondary phases, and improve the solar cell properties in general. Further research was carried out to assess the efficiency of solar cells made from Cu_2ZnSnS_4 monograin powders grown in molten LiI, NaI, KI, RbI and CsI. Figure 3.7 shows the respective influence of the used flux materials to the MGL solar cell parameters: short circuit current densitry (J_{sc}), open circuit voltage (V_{oc}), fill factor (*FF*), and the efficiency (*PCE*) values are displayed as box plots. Data are extrapolated from the analysis of 10 solar cells.

The power conversion efficeincy in case of all five materials is as follows: CsI (0.01%), RbI (5.52%), LiI (4.52%), NaI (4.96 %) and KI (6.12%). Fill factor and short circuit current density also varied in values. Solar cells based on KI grown powder showed the highest and in the case of CsI the lowest parameters. Furthermore, the V_{oc} in case of

CsI was the lowest one and LiI illustrate the highst value of 681 mV. However, the average V_{oc} values except for CsI, in case of all other flux materials are in the same range with little varitations. The V_{oc} values of the devices based on RbI, LiI and KI remained at the level 670-681 mV. The solar cells based on NaI grown power showed 40 mV decrease in V_{oc} values (630 mV). The RbI, NaI and KI depicts the same range of J_{sc}, KI shows the highest and CsI shows the lowest values. As discussed in the EDX results part 3.2 (shown in Figure 3.2), the CZTS material grown in CsI resulted in the stoichometric elemental composition. Therefore, due to the final stoichiometrical composition of powder, it could be possible that the material grown in CsI does not work in solar cells. A copper poor and zinc rich composition has been established to be good for solar cell performance.

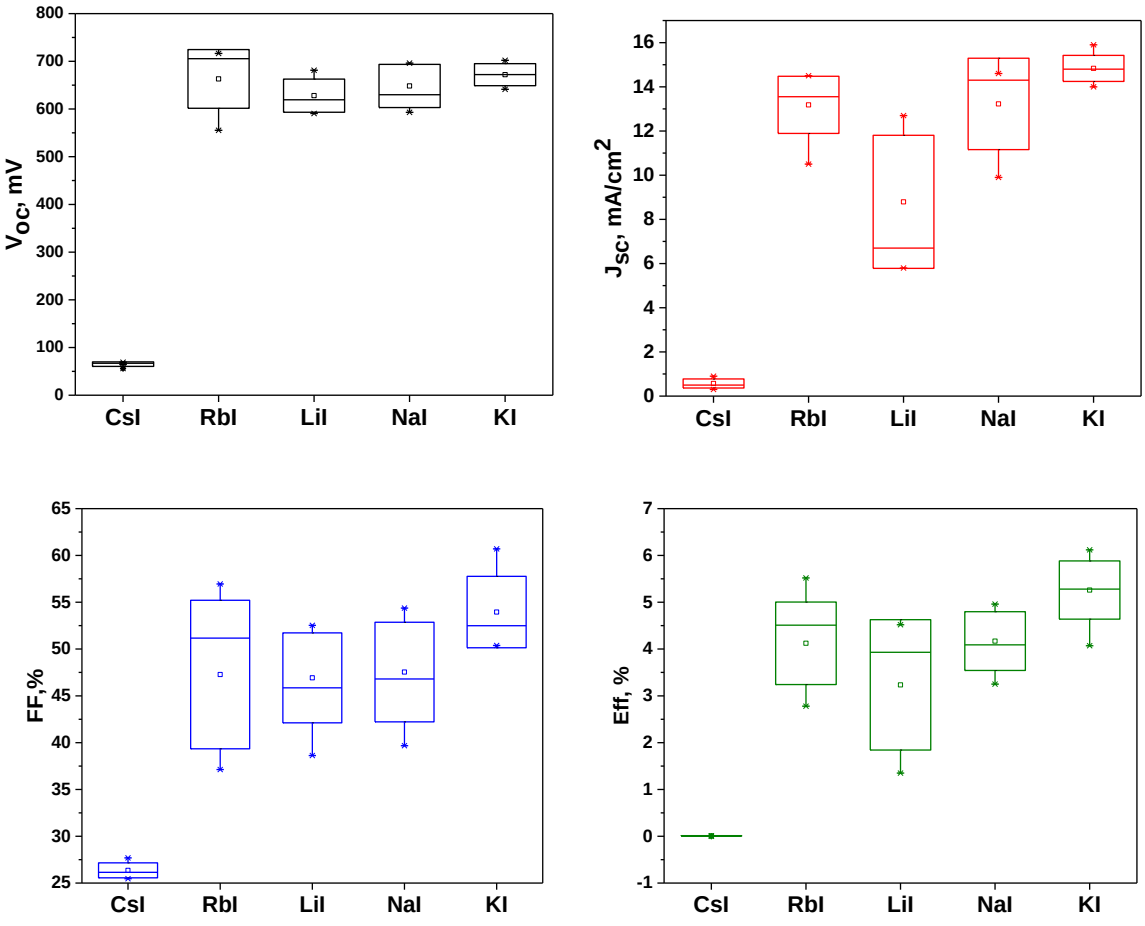

Figure 3.7 Solar cell parameters of Cu_2ZnSnS_4 monograin powders grown in CsI, RbI, LiI, NaI and KI molten salts.

Figure 3.8 illustrates *J-V* characteristics for the devices based on the CZTS monograin powders synthesized in CsI, RbI, LiI, NaI, KI molten salts, which are selected on the basis of the highest efficiency values and corresponding output parameters are listed in the Table 3.2.

Figure 3.8 and Table 3.2 clearly demonstrates that in the case of potassium iodide (KI) J_{SC} exhibits the highest value that is 14.9 mA/cm^2 and also highest *FF* value 60.7 %. The V_{oc} is 677 mV, that is slightly lower compared with the LiI based MGL solar cell (V_{oc} = 681 mV). The monograin layer solar cells prepared from Cu_2ZnSnS_4 powders grown in potassium iodide (KI) flux presented the best solar cell efficiency of 6.12%.

For the given technological conditions in this exeprimental work, KI has been demonstrated to be the most useful flux material to enhance PV performance of CZTS and CsI has been demostrated the most unsuitable.

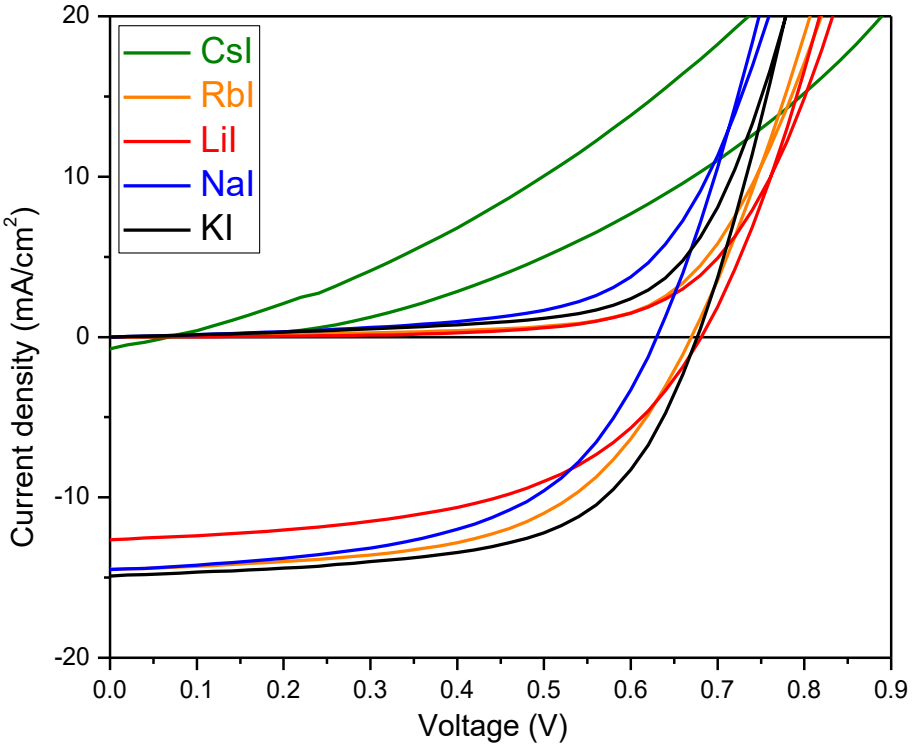

Figure 3.8 *J-V* chracteristics of the best performing Cu_2ZnSnS_4 solar cells based on absorber material synthsized in CsI, RbI, LiI, NaI and KI molten salts.

Tabel 3.2 *J-V* curve parameters of the best performing Cu_2ZnSnS_4 MGL solar cells in dependence of used flux material CsI, RbI, LiI, NaI and KI.

Flux material	***V*$_{oc}$, mV**	***FF*, %**	***J*$_{sc}$, mA/cm^2**	**Efficiency, %**
CsI	67	27.69	0.7	0.01
RbI	670	56.95	14.5	5.52
LiI	681	52.53	12.6	4.52
NaI	630	54.38	14.5	4.96
KI	677	60.70	14.9	6.12

3.4.2 External quantum efficiency (EQE)

External quantum efficiency analysis was used for evaluation of the effective bandgap energy (E_g*) of the absorber materials because assesment of E_g from the optical absorption or reflectance spectra of monograin powders is tricky. The effective bandgap energy can be evaluated from the linear segment of the low-energy side of the construction $(EQE)^2$ *vs* E curves [73]. Figure 3.9 illustrates how the different flux materials influence the effective bandgap energy values of CZTS monograin powders. As the EQE signal for CsI grown powder was very low, the evaluation of E_g* was not possible. The observed E_g* values for CZTS monograin powders grown in RbI, NaI and KI were 1.569 eV, 1.571 eV and 1.568 eV, respectively. The CZTS powder grown in LiI depicts the highest E_g* value (1.661 eV). The increase in bandgap energy value indicates to the Li incorporation from LiI into the crystal lattice of CZTS forming new $(Cu_{1-x}Li_x)_2ZnSnS_4$ solid solution where part of the Cu is replaced with Li. This result is in a good correlation with XRD analysis, where the shift in diffraction peaks positions and increase in crystal lattice parameters was obtained.

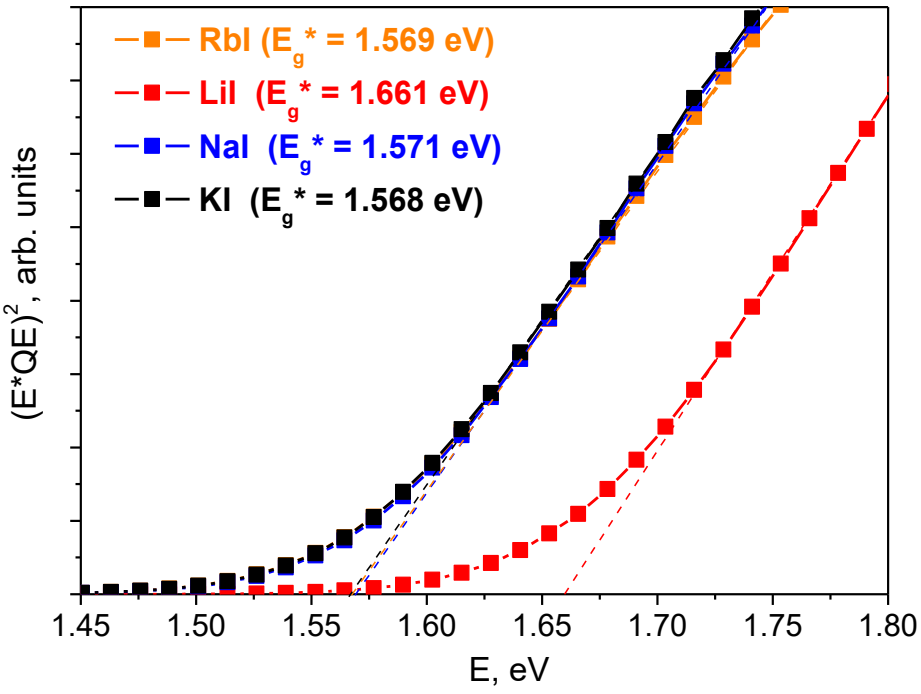

Figure 3.9 Effective bandgap energy values of Cu_2ZnSnS_4 monograin powders grown in RbI, LiI, NaI and KI molten salts.

SUMMARY

The objective of this master thesis was the characterization of Cu_2ZnSnS_4 (CZTS) monograin powders properties grown in different molten salts (as flux materials) and to study the effect of used flux material to the performance of monograin layer solar cells. Five $Cu_{1.85}Zn_{1.1}SnS_{4.12}$ powder materials were synthesized from binary compounds CuS (5N), ZnS (5N), SnS (5N) and elemental sulfur (5N) by isothermal synthesis-growth method at 740°C for 136 hours in the liquid phase of cesium iodide (CsI), rubidium iodide (RbI), lithium iodide (LiI), sodium iodide (NaI) and potassium iodide (KI).

- SEM images showed a significant difference in the size and morphology of CZTS monograin powder particles grown in different molten salts. CZTS powder grown in CsI molten salt resulted in uniform and non-aggregated crystals with smooth facets and roundy edges, whereas the growth in RbI resulted in cystals with uneven edges, irregularities of porous surface and shape. By using LiI as flux material SEM analysis revealed well-formed individual roundy crystals. CZTS powder grown in NaI consisted of non-aggregated crystals with flat and smooth surfaces and sintered crystals. The growth of CZTS in KI molten salt resulted in different and uneven shape of crystals. Mainly agglomerated crystals with rough and porous edges were formed.

- EDX analysis revealed that there are differences between the input composition ($Cu_{1.85}Zn_{1.1}SnS_{3.95}$) and the obtained composition of CZTS monograin powders synthesized in different molten salts. A copper poor and zinc rich composition of CZTS was obtained by using RbI, LiI, NaI or KI as flux material, whereas in the case of CsI the produced monograin powder showed nearly stoichiometric chemical composition.

- XRD analysis confirmed the Li incorporation into CZTS monograin powder crystals. XRD pattern of powder grown in LiI revealed a shift of the diffraction peaks toward lower angles and an increase in lattice parameters, indicating to the lattice expansion.

- Raman analysis showed that the half width at half maximum (hwhm) of the main A1 peak was varying by varying the flux material. Monograin powders grown in LiI showed the widest mode of the main Raman peak (hwhm= 3.55 cm^{-1}). This finding supports the XRD results and indicates also to the incorporation of Li from LiI into the crystal lattice. In case of CsI and RbI Raman peaks are sharp and

narrow with hwhm of 2.25 and 2.81 cm^{-1}, respectively, showing a higher level of crystallinity compared to other produced powders.

- The EQE analysis showed different effective bandgap energy values of CZTS MGPs grown in different molten fluxes. The evaluation of *Eg** was not possible in the case of CsI due to the low intensity of EQE signal. The observed *Eg** values for CZTS monograin powders grown in RbI, NaI and KI were 1.569 eV, 1.571 eV and 1.568 eV, respectively. The CZTS powder grown in LiI depicts the highest Eg* value (1.661 eV). The increase in bandgap energy value indicates to the Li incorporation from LiI into the crystal lattice of CZTS forming new $(Cu_{1-x}Li_x)_2ZnSnS_4$ solid solution.

- The MGL solar cells produced from Cu_2ZnSnS_4 powders grown in potassium iodide (KI) flux presented the best solar cell efficiency of 6.12%.

LIST OF REFERENCES

[1] C. P. Poole and J. J. Frank Owens, "INTRODUCTION TO NANOTECHNOLOGY Library of Congress Cataloging-in-Publication Data," [Online]. Available: https://startinnovationblog.files.wordpress.com/2015/12/nanotechnology-by-charlespoole.pdf.

[2] S. R. Bull, "Renewable energy today and tomorrow," *Proc. IEEE*, vol. 89, no. 8, pp. 1216–1226, 2001, doi: 10.1109/5.940290.

[3] N. Kannan and D. Vakeesan, "Solar energy for future world: - A review," *Renew. Sustain. Energy Rev.*, vol. 62, pp. 1092–1105, 2016, doi: 10.1016/j.rser.2016.05.022.

[4] F. Liu, W. Wang, L. Wang, and G. Yang, "Ferroelectric-semiconductor photovoltaics: Non-PN junction solar cells," *Appl. Phys. Lett.*, vol. 104, no. 10, pp. 1–5, 2014, doi: 10.1063/1.4868304.

[5] F. Ahmad, A. Lakhtakia, T. H. Anderson, and P. B. Monk, "Towards highly efficient thin-film solar cells with a graded-bandgap CZTSSe layer Journal of Physics: Energy Corrigendum: Towards highly efficient thin-film solar cells with a Towards highly efficient thin-film solar cells with a graded-bandgap CZTSSe layer," *J. Phys. Energy*, vol. 2, p. 25004, 2020, doi: 10.1088/2515-7655/ab8913.

[6] A. Luque and S. Hegedus, *Handbook of Photovoltaic Science and Engineering*. 2011.

[7] "How Photovoltaic Cells Generate Electricity." https://www.imagesco.com/articles/photovoltaic/photovoltaic-pg4.html (accessed Apr. 13, 2021).

[8] A. Mavlonov *et al.*, "A review of Sb2Se3 photovoltaic absorber materials and thin-film solar cells," *Sol. Energy*, vol. 201, no. February, pp. 227–246, 2020, doi: 10.1016/j.solener.2020.03.009.

[9] M. Deshpande and R. Seyezhai, "REVIEW OF HYBRID SOLAR CELLS BASED ON CdSe AND TiO_2 MATERIALS," pp. 3387–3392, 2014.

[10] A. Niv, Z. R. Abrams, M. Gharghi, C. Gladden, and X. Zhang, "Overcoming the bandgap limitation on solar cell materials," *Appl. Phys. Lett.*, vol. 100, no. 8, 2012, doi: 10.1063/1.3682101.

[11] K. Ito and T. Nakazawa, "Electrical and optical properties of stannite-type quaternary semiconductor thin films," *Jpn. J. Appl. Phys.*, vol. 27, no. 11R, pp. 2094–2097, 1988, doi: 10.1143/JJAP.27.2094.

[12] H. Katagiri, N. Sasaguchi, S. Hando, S. Hoshino, J. Ohashi, and T. Yokota, "Preparation and evaluation of Cu_2ZnSnS_4 thin films by sulfurization of E-B evaporated precursors," *Sol. Energy Mater. Sol. Cells*, vol. 49, no. 1–4, pp. 407–414, 1997, doi: 10.1016/S0927-0248(97)00119-0.

[13] H. Katagiri *et al.*, "Development of CZTS-based thin film solar cells," *Thin Solid Films*, vol. 517, no. 7, pp. 2455–2460, 2009, doi: 10.1016/j.tsf.2008.11.002.

[14] W. Wang *et al.*, "Device characteristics of CZTSSe thin-film solar cells with

12.6% efficiency," *Adv. Energy Mater.*, vol. 4, no. 7, pp. 1–5, 2014, doi: 10.1002/aenm.201301465.

[15] M. R. Ananthan and B. Mahalaksmi, "Review on CZTS based solar cells," *Adv. Nat. Appl. Sci.*, vol. 8, p. 72+, Apr. 2014.

[16] I. Repins *et al.*, "Co-evaporated $Cu_2ZnSnSe_4$ films and devices," *Sol. Energy Mater. Sol. Cells*, vol. 101, pp. 154–159, 2012, doi: 10.1016/j.solmat.2012.01.008.

[17] D. Wang, W. Zhao, Y. Zhang, and S. (Frank) Liu, "Path towards high-efficient kesterite solar cells," *J. Energy Chem.*, vol. 27, no. 4, pp. 1040–1053, 2018, doi: 10.1016/j.jechem.2017.10.027.

[18] M. P. Suryawanshi *et al.*, "Materials Technology Advanced Performance Materials CZTS based thin film solar cells: a status review CZTS based thin film solar cells: a status review," doi: 10.1179/1753555712Y.0000000038.

[19] M. Grossberg *et al.*, "The electrical and optical properties of kesterites," *JPhys Energy*, vol. 1, no. 4, Oct. 2019, doi: 10.1088/2515-7655/ab29a0.

[20] S. A. Eshraghi, S. Kianian, B. Ostrom, O. M. Stafsudd, and A. L. Gentile, "The electrical and optical properties of n-type HgIn2Te4," *Phys. Status Solidi*, vol. 105, no. 2, pp. 563–566, 1988, doi: 10.1002/pssa.2211050230.

[21] S. Chen, X. G. Gong, A. Walsh, and S. H. Wei, "Defect physics of the kesterite thin-film solar cell absorber Cu_2ZnSnS_4," *Appl. Phys. Lett.*, vol. 96, no. 2, pp. 4–7, 2010, doi: 10.1063/1.3275796.

[22] A. Walsh, S. Chen, X. G. Gong, and S. H. Wei, "Crystal structure and defect reactions in the kesterite solar cell absorber Cu_2ZnSnS_4 (CZTS): Theoretical insights," *AIP Conf. Proc.*, vol. 1399, no. 2011, pp. 63–64, 2011, doi: 10.1063/1.3666258.

[23] K. Biswas, S. Lany, and A. Zunger, "The electronic consequences of multivalent elements in inorganic solar absorbers: Multivalency of Sn in Cu_2ZnSnS_4," *Appl. Phys. Lett.*, vol. 96, no. 20, pp. 2–5, 2010, doi: 10.1063/1.3427433.

[24] S. G. Haass *et al.*, "Complex Interplay between Absorber Composition and Alkali Doping in High-Efficiency Kesterite Solar Cells," *Adv. Energy Mater.*, vol. 8, no. 4, pp. 1–9, 2018, doi: 10.1002/aenm.201701760.

[25] Y. E. Romanyuk *et al.*, "Doping and alloying of kesterites," *J. Phys. Energy*, vol. 1, no. 4, p. 044004, 2019, doi: 10.1088/2515-7655/ab23bc.

[26] D. S. Dhawale, A. Ali, and A. C. Lokhande, "Impact of various dopant elements on the properties of kesterite compounds for solar cell applications: A status review," *Sustain. Energy Fuels*, vol. 3, no. 6, pp. 1365–1383, 2019, doi: 10.1039/c9se00040b.

[27] A. Cabas-Vidani *et al.*, "High-Efficiency $(LixCu1-x)_2ZnSn(S,Se)_4$ Kesterite Solar Cells with Lithium Alloying," *Adv. Energy Mater.*, vol. 8, no. 34, pp. 1–8, 2018, doi: 10.1002/aenm.201801191.

[28] W. Li *et al.*, "Revealing the Role of Potassium Treatment in CZTSSe Thin Film Solar Cells," *Chem. Mater.*, vol. 29, no. 10, pp. 4273–4281, 2017, doi: 10.1021/acs.chemmater.7b00418.

[29] Y. Wu *et al.*, "The effect of Rb doping on CZTSSe solar cells," *Sol. Energy*, vol. 187, no. March, pp. 269–273, 2019, doi: 10.1016/j.solener.2019.05.027.

[30] A. S. Ionkin, B. M. Fish, W. J. Marshall, and R. H. Senigo, "Use of inorganic fluxes to control morphology and purity of crystalline késterite and related quaternary chalcogenides," *Sol. Energy Mater. Sol. Cells*, vol. 104, pp. 23–31, Sep. 2012, doi: 10.1016/j.solmat.2012.04.042.

[31] B. Unveroglu and G. Zangari, " Photoelectrochemical Behavior of Bismuth-Containing Cu $_2$ZnSnS$_4$ (CZTS) Absorber Layers for Photovoltaic Applications ," *J. Electrochem. Soc.*, vol. 166, no. 5, pp. H3040–H3046, 2019, doi: 10.1149/2.0081905jes.

[32] M. Mousel *et al.*, "Cu-Rich Precursors Improve Kesterite Solar Cells," *Adv. Energy Mater.*, vol. 4, no. 2, p. 1300543, Jan. 2014, doi: 10.1002/aenm.201300543.

[33] X. Song, X. Ji, M. Li, W. Lin, X. Luo, and H. Zhang, "A review on development prospect of CZTS based thin film solar cells," *International Journal of Photoenergy*, vol. 2014. Hindawi Publishing Corporation, 2014, doi: 10.1155/2014/613173.

[34] W. C. Hsu *et al.*, "The effect of Zn excess on kesterite solar cells," *Sol. Energy Mater. Sol. Cells*, vol. 113, pp. 160–164, 2013, doi: 10.1016/j.solmat.2013.02.015.

[35] S. Schorr, A. Weber, V. Honkimäki, and H. W. Schock, "In-situ investigation of the kesterite formation from binary and ternary sulphides," *Thin Solid Films*, vol. 517, no. 7, pp. 2461–2464, Feb. 2009, doi: 10.1016/j.tsf.2008.11.053.

[36] F. Biccari *et al.*, "Fabrication of Cu_2ZnSnS_4 solar cells by sulfurization of evaporated precursors," *Energy Procedia*, vol. 10, pp. 187–191, 2011, doi: 10.1016/j.egypro.2011.10.175.

[37] K. Muska, M. Kauk, M. Altosaar, M. Pilvet, M. Grossberg, and O. Volobujeva, "Synthesis of Cu_2ZnSnS_4 monograin powders with different compositions," *Energy Procedia*, vol. 10, pp. 203–207, 2011, doi: 10.1016/j.egypro.2011.10.178.

[38] M. A. Green, "Photovoltaic principles," in *Physica E: Low-Dimensional Systems and Nanostructures*, Apr. 2002, vol. 14, no. 1–2, pp. 11–17, doi: 10.1016/S1386-9477(02)00354-5.

[39] E. Mellikov *et al.*, "Monograin materials for solar cells," *Sol. Energy Mater. Sol. Cells*, vol. 93, no. 1, pp. 65–68, Jan. 2009, doi: 10.1016/j.solmat.2008.04.018.

[40] G. Nkwusi *et al.*, "FORMATION OF COPPER ZINC TIN SULFIDE IN CADMIUM IODIDE FOR MONOGRAIN MEMBRANE SOLAR CELLS," vol. 2, pp. 1–10, 2012.

[41] H. Wang, "Progress in thin film solar cells based on Cu_2ZnSnS_4," *Int. J. Photoenergy*, vol. 2011, no. Figure 2, 2011, doi: 10.1155/2011/801292.

[42] M. Science, "Comparative Study of $Cu_2ZnSnSe_4$ Monograin Powder Synthesis in Different Molten Salts Monoterapulbrilise Cu 2 ZnSnSe 4 sünteeskasvatuse võrdlus," 2015.

[43] R. Lechner *et al.*, "$Cu_2ZnSn(S,Se)_4$ solar cells processed by rapid thermal

processing of stacked elemental layer precursors," *Thin Solid Films*, vol. 535, no. 1, pp. 5–9, 2013, doi: 10.1016/j.tsf.2012.10.042.

[44] R. Adhi Wibowo, W. Hwa Jung, and K. H. Kim, "Synthesis of $Cu_2ZnSnSe_4$ compound powders by solid state reaction using elemental powders," *J. Phys. Chem. Solids*, vol. 71, no. 12, pp. 1702–1706, 2010, doi: 10.1016/j.jpcs.2010.08.012.

[45] K. Muska, M. Kauk, M. Grossberg, M. Altosaar, J. Raudoja, and O. Volobujeva, "Influence of compositional deviations on the properties of $Cu_2ZnSnSe_4$ monograin powders," *Energy Procedia*, vol. 10, pp. 323–327, 2011, doi: 10.1016/j.egypro.2011.10.198.

[46] E. Mellikov *et al.*, "Monograin materials for solar cells," *Sol. Energy Mater. Sol. Cells*, vol. 93, no. 1, pp. 65–68, 2009, doi: 10.1016/j.solmat.2008.04.018.

[47] J. Hiie, M. Altosaar, E. Mellikov, P. Kukk, J. Sapogova, and D. Meissner, "Growth of CdTe monograin powders," *Phys. Scr. T*, vol. T69, pp. 155–158, 1997, doi: 10.1088/0031-8949/1997/t69/028.

[48] I. Leinemann *et al.*, "Comparison of Copper Zinc Tin Selenide Formation In Molten Potassium Iodide and Sodium Iodide As Flux Material," *Conf. Young Sci. Energy Issues*, vol. 8, no. May, p. 326, 2011.

[49] K. Timmo *et al.*, "The effect of Ag alloying of $Cu_2(Zn,Cd)SnS_4$ on the monograin powder properties and solar cell performance," *J. Mater. Chem. A*, vol. 7, no. 42, pp. 24281–24291, 2019, doi: 10.1039/c9ta07768e.

[50] K. Timmo *et al.*, "$Cu(In,Ga)Se_2$ monograin powders with different Ga content for solar cells," *Sol. Energy*, vol. 176, no. July, pp. 648–655, 2018, doi: 10.1016/j.solener.2018.10.078.

[51] M. Kauk-Kuusik *et al.*, "Study of $Cu_2CdGeSe_4$ monograin powders synthesized by molten salt method for photovoltaic applications," *Thin Solid Films*, vol. 666, no. August, pp. 15–19, 2018, doi: 10.1016/j.tsf.2018.09.025.

[52] K. Timmo *et al.*, "Sulfur-containing $Cu_2ZnSnSe_4$ monograin powders for solar cells," *Sol. Energy Mater. Sol. Cells*, vol. 94, no. 11, pp. 1889–1892, 2010, doi: 10.1016/j.solmat.2010.06.046.

[53] I. Leinemann *et al.*, "Reaction enthalpies of $Cu_2ZnSnSe_4$ synthesis in KI," *J. Therm. Anal. Calorim.*, vol. 119, no. 3, pp. 1555–1564, 2015, doi: 10.1007/s10973-014-4339-5.

[54] I. Leinemann *et al.*, "$Cu_2ZnSnSe_4$ formation and reaction enthalpies in molten NaI starting from binary chalcogenides," *J. Therm. Anal. Calorim.*, vol. 118, no. 2, pp. 1313–1321, 2014, doi: 10.1007/s10973-014-4102-y.

[55] K. Timmo *et al.*, "Comparative study of SnS recrystallization in molten CdI2, SnCl2and KI," *Phys. Status Solidi Curr. Top. Solid State Phys.*, vol. 13, no. 1, pp. 8–12, 2016, doi: 10.1002/pssc.201510082.

[56] K. L. Juhasz, P. Baumli, and G. Kaptay, "Fabrication of carbon fibre reinforced, aluminium matrix composite by potassium iodide (KI) - Potassium hexafluoro-titanate (K 2TiF 6) flux," *Materwiss. Werksttech.*, vol. 43, no. 4, pp. 310–314, 2012, doi: 10.1002/mawe.201200946.

[57] Y. Lin, Z. Wen, J. Liu, D. Wu, P. Zhang, and J. Zhao, "Constructing a uniform lithium iodide layer for stabilizing lithium metal anode," *J. Energy Chem.*, vol. 55, pp. 129–135, 2021, doi: 10.1016/j.jechem.2020.07.003.

[58] "Sodium iodide Formula - Sodium Iodide Uses, Properties, Structure and Formula." https://www.softschools.com/formulas/chemistry/sodium_iodide_formula/300/ (accessed Apr. 13, 2021).

[59] "Lithium iodide | LiI - PubChem." https://pubchem.ncbi.nlm.nih.gov/compound/Lithium-iodide (accessed Apr. 13, 2021).

[60] "Cesium Iodide | AMERICAN ELEMENTS ®." https://www.americanelements.com/cesium-iodide-7789-17-5 (accessed Apr. 13, 2021).

[61] N. Cameli, F. Bardazzi, R. Morelli, and A. Tosti, "Contact dermatitis from rubidium iodide in eyedrops," *Contact Dermatitis*, vol. 23, no. 5, pp. 377–378, 1990, doi: 10.1111/j.1600-0536.1990.tb05182.x.

[62] "Rubidium Iodide | AMERICAN ELEMENTS ®." https://www.americanelements.com/rubidium-iodide-7790-29-6 (accessed May 03, 2021).

[63] "Potassium iodide | KI - PubChem." https://pubchem.ncbi.nlm.nih.gov/compound/Potassium-iodide (accessed May 03, 2021).

[64] X. Li *et al.*, "Effect of absorber surface modification on the optoelectronic properties of $Cu_2CdGeSe_4$ solar cells.," *Thin Solid Films*, vol. 697, p. 137822, Mar. 2020, doi: 10.1016/j.tsf.2020.137822.

[65] M. Danilson, *Temperature Dependent Electrical Properties of Kesterite Monograin Layer Solar Cells*. 2016.

[66] W. Zhou, R. Apkarian, Z. L. Wang, and D. Joy, "Fundamentals of scanning electron microscopy (SEM)," *Scanning Microsc. Nanotechnol. Tech. Appl.*, pp. 1–40, 2007, doi: 10.1007/978-0-387-39620-0_1.

[67] "Scanning Electron Microscopy (SEM)." https://serc.carleton.edu/research_education/geochemsheets/techniques/SEM.html (accessed Apr. 11, 2021).

[68] "Energy-Dispersive X-Ray Spectroscopy - an overview | ScienceDirect Topics." https://www.sciencedirect.com/topics/materials-science/energy-dispersive-x-ray-spectroscopy (accessed Apr. 11, 2021).

[69] H. G. M. Edwards, *Modern Raman spectroscopy—a practical approach.Ewen Smith and Geoffrey Dent. John Wiley and Sons Ltd, Chichester, 2005. Pp. 210. ISBN 0 471 49668 5 (cloth, hb); 0 471 49794 0 (pbk)*, vol. 36, no. 8. 2005.

[70] "Raman Spectroscopy - an overview | ScienceDirect Topics." https://www.sciencedirect.com/topics/neuroscience/raman-spectroscopy (accessed Apr. 11, 2021).

[71] "X-ray Powder Diffraction (XRD)." https://serc.carleton.edu/research_education/geochemsheets/techniques/XRD.html (accessed May 03, 2021).

[72] "Solar Cell Parameters and Equivalent Circuit 9.1 External solar cell parameters."

[73] J. Krustok, R. Josepson, T. Raadik, and M. Danilson, "Potential fluctuations in $Cu_2ZnSnSe_4$ solar cells studied by temperature dependence of quantum efficiency curves," *Phys. B Condens. Matter*, vol. 405, no. 15, pp. 3186–3189, 2010, doi: 10.1016/j.physb.2010.04.041.

[74] A. Lafond, C. Guillot-Deudon, J. Vidal, ‖ M Paris, C. La, and S. Jobic, "Substitution of Li for Cu in Cu_2ZnSnS_4 : Toward Wide Band Gap Absorbers with Low Cation Disorder for Thin Film Solar Cells," *Inorg. Chem*, vol. 56, 2017, doi: 10.1021/acs.inorgchem.6b02865.

[75] P. A. Fernandes, P. M. P. Salomé, and A. F. da Cunha, "Growth and Raman scattering characterization of Cu_2ZnSnS_4 thin films," *Thin Solid Films*, vol. 517, no. 7, pp. 2519–2523, 2009, doi: 10.1016/j.tsf.2008.11.031.

[76] M. Y. Valakh *et al.*, "Raman scattering and disorder effect in Cu_2ZnSnS_4," *Phys. Status Solidi - Rapid Res. Lett.*, vol. 7, no. 4, pp. 258–261, 2013, doi: 10.1002/pssr.201307073.

[77] M. Grossberg, J. Krustok, J. Raudoja, K. Timmo, M. Altosaar, and T. Raadik, "Photoluminescence and Raman study of $Cu_2ZnSn(Se\ xS1 - X)_4$ monograins for photovoltaic applications," *Thin Solid Films*, vol. 519, no. 21, pp. 7403–7406, 2011, doi: 10.1016/j.tsf.2010.12.099.

[78] H. Yoo and J. Kim, "Comparative study of Cu_2ZnSnS_4 film growth," *Sol. Energy Mater. Sol. Cells*, vol. 95, no. 1, pp. 239–244, 2011, doi: 10.1016/j.solmat.2010.04.060.